MULTIPAYLOAD SOUNDING ROCKET OBSERVATIONS OF VELOCITY SHEAR, VLF HISS, AND ALFVÉN WAVES

A Dissertation

Presented to the Faculty of the Graduate School

of Cornell University

in Partial Fulfillment of the Requirements for the Degree of

Doctor of Philosophy

by

Erik Thomas Lundberg

January 2012

MULTIPAYLOAD SOUNDING ROCKET OBSERVATIONS OF VELOCITY SHEAR, VLF HISS, AND ALFVÉN WAVES

Erik Thomas Lundberg, Ph.D.

Cornell University 2012

The multipayload Cascades2 sounding rocket was launched on March 20th, 2009 at 11:04:00 UT into a pre-midnight poleward boundary intensification. Three papers are presented from two different time periods of the flight. On the upleg the payload array encountered a region of VLF hiss. During this time period the interpayload separation vector between two wireboom subpayloads was nearly aligned to $\mathbf{B}_0$. This configuration was sufficient to directly measure the parallel wavelength of VLF hiss and create upper and lower bound estimates for the perpendicular wavelength. For the ~ 60km preceding entry into the polar cap the payload array encountered a region of intense, Alfénic aurora which was characterized by large, fluctuating DC electric and magnetic fields, field-aligned auroral electron bursts, broadband extremely low frequency plasma wave emissions and elevated ion temperatures. A fully spatial analysis of the DC electric field signals was used to measure velocity shears of +/- 6Hz, a factor of two lower than single payload measurement of the same data would imply, but sufficient to drive electrostatic plasma wave emissions. An interferometric spatio-temporal analysis revealed that kilometer scale electromagentic disturbances were moving at ~ 8km/s across the payloads, which was similar to the velocity of tall aurora rays observed in optical aurora. Analysis of the power spectral density from the DC electric field found two break points in the spectral slope. The first breakpoint occurred near $k\lambda_e > 1$, where λ_e is

the electron inertial length. The second breakpoint occurred at kρ_s = 1 where ρ_s is the acoustic radius at electron temperature. Spectral fits were performed which revealed power laws of $k^{-1.77}$ from DC to the first breakpoint, k^{-5} from the first breakpoint to the second breakpoint, and k^{-2} beyond the second breakpoint. The noisier fluctuating magnetic field spectra also followed a power law. A fit to these data reveals a $k^{-2.37}$ power law. A polarization analysis of the despun DC electric field signals revealed that at scales longer than ρ_s the observed fluctuations were well described as plane waves, and at scales shorter than ρ_s observed BB-ELF were not well described as plane waves indicating they were Doppler shifted spatial structures.

BIOGRAPHICAL SKETCH

Erik Thomas Lundberg entered the world two months early into the cold, dark Minneapolis winter to the joy of his parents Thomas and Mary Lou Lundberg. After a lackluster high school career that focussed primarily on soccer, cross-country, track and videogames Erik graduated from Mounds View High School in Arden Hills, MN in the Spring of 2002. The next autumn Erik entered Augsburg College where he studied Physics and Mathematics and ran on the cross-country, indoor and outdoor track and field teams. Erik graduated from Augsburg College in 2006 with Honors and earned a BS in Physics and a BA in Mathematics. In July 2006 Erik packed his suitcase and jumped on a plane to Ithaca, NY where he entered the Ms/PhD program in Electrical and Computer Engineering under the advisement of Professor Paul Kintner. In May 2010 Erik earned his MS by passing the last A-exam administered by Professor Kintner. Erik has two younger siblings. His sister, Britta, is three years younger and finished her first year of graduate school at the Univerisity of Michigan in Materials Science. His brother, Anders, has finished his third year of undergraduate and studies Mechanical Engineering at Montana State University at Bozeman. Erik will finish the requirements for his PhD in the fall of 2011.

ACKNOWLEDGEMENTS

First and foremost I would like to thank my officemates, Asti Bhatt, Alessandro Cerruti and particularly Brady O'Hanlon. As a result of us always working on different things you challenged me to explain myself in somewhat coherent terms and allowed me to develop my creativity. Second I want to thanks my friends in the greater Cornell community and Ithaca area. Ben Clarke, Rich McCloskey and Leslie Clarke are some of the best and most supportive friends and roommates someone could ask for. Special thanks to Ben and Leslie's dogs Watson and Ginny for teaching me that neither puppies nor littermates were appropriate pets for me. My parents, Thomas and Mary Lou Lundberg, deserve extra parenting points for allowing me to find my own way and supporting all of my decisions and helping me develop the maturity to, often, make the correct ones.

My committee members each contributed to my development in different ways. In addition to great teaching, Dave Hysell did a great job stepping in for Paul at the last minute and continues to provide a template for a scientist who wants to "do it all". Charlie Seyler demonstrated both how to approach problems in plasma physics and how to let your work speak for itself – a trait that is increasingly lost. Mike Kelley is the exemplar ionospheric physicist whose contributions speak for themselves. Finally, to my true adviser, Paul Kintner thank you for making me become and expert in many things. Thanks for showing me how to make significant contributions and think on my feet. Finally, thank you for demonstrating how a scientist is also a citizen.

Having my adviser, Paul Kintner, die during my last year of studies presented difficulties beyond above and beyond those encountered my a "typical" rocket student. Steve Powell has all of my gratitude for being extremely sup-

Figure 1: From left to right, the author (Erik Lundberg), the adviser (Paul Kintner) and the engineer (Steve Powell).

portive during this. During my 5 years at Cornell I spent more time with Steve than any other person and this has shaped me both as an engineer and as a man. I can't put words on how important Steve has been to my development. There is no way I would have graduated without him and his support. Figure 1 shows Steve, Paul and I in front of the SCIFER-2 sounding rocket payload. This was the last sounding rocket that Paul was a PI on, and I am extremely grateful that I was able to work on it.

TABLE OF CONTENTS

LIST OF TABLES

LIST OF FIGURES

CHAPTER 1

MULTI-PAYLOAD MEASUREMENT OF TRANSVERSE VELOCITY SHEARS IN THE TOPSIDE IONOSPHERE

1.1 Abstract

Using a multi-payload sounding rocket mission, we present the first direct measurement of velocity shear in the topside auroral ionosphere. In regions of large,~ 200 mV/m, transient electric fields we directly measure differences in the plasma drift velocity. From these differences, shear frequencies reaching +/−6Hz are measured. These directly measured shears are compared with the shear inferred from single payload measurements. It is shown this traditional measurement of shear overestimates the shear frequency by a factor of two for this event, highlighting the importance of the temporal component of near-DC electric field structures. Coincident with these strong fields and shears are enhanced emissions of broadband, extremely low frequency (BB-ELF) plasma waves, and a narrowband wave emission near the H^+-O^+ bi-ion resonant frequency.

1.2 Introduction

Observations of inferred shear in transverse flows in the topside ionosphere associated with auroral activity have been reported for at least three decades [*Kelley and Carlson*, 1977], and in the auroral acceleration region slightly earlier [*Kintner*, 1976]. Units of velocity shear, $f_s = |\partial V_x/\partial x|$, are Hz, which is con-

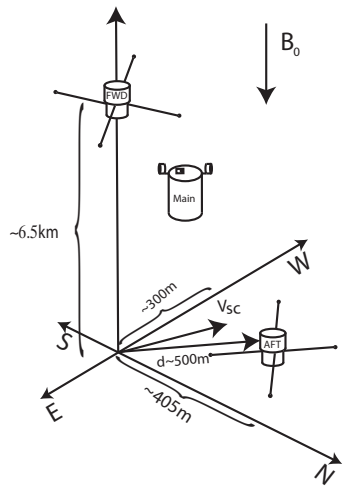

Figure 1.1: A cartoon illustrating the configuration of the payloads (not to scale), the coordinate systems, and the geometry of the shear measurement.

venient for comparison between different space plasmas and with laboratory plasmas. Typical inferred shear frequencies measured in the auroral zone are of the order $0.1\Omega_i$, where $\Omega_i = 2\pi f_{ci}$ is the ion cyclotron frequency (see review by *Amatucci* [1999]). The main drawback to these single point measurements is their assumption of stationarity in the plasma frame, i.e. that variations in the measured electric field are entirely due to the spacecraft passing through spatial structures. Using this assumption shear has been inferred by differencing subsequent electric field measurements and dividing by the distance the spacecraft traveled between each measurement. Often, this has been further simplified to the very rough approximation $f_s \simeq V_e^0/L$, where V_e^0 is the E × B drift velocity, and L is shear region scale size determined by the spacecraft velocity and traversal time.

In their landmark paper, *Kindel and Kennel* [1971] predict the instability of O^+ and H^+ electrostatic ion cyclotron (EIC), and ion acoustic waves, due to field aligned currents in the topside auroral ionosphere. The EIC waves are

distinguished by their structure at and near multiples of the ion gyrofrequencies which allows the waves to gyroresonantly interact with and heat ionospheric ions. This efficient heating gives this instability special importance and it has subsequently been termed the current driven electrostatic ion cyclotron (CDEIC) instability.

There have been sounding rocket observations of plasma wave emissions with structure at or near multiples of Ω_{H^+} in the auroral ionosphere which have been identified as ion-Bernstein mode waves (*Mosier and Gurnett* [1969],*Kintner et al.* [1991]). Magnetospheric observations of H^+ cyclotron waves have been more common, and their growth has been attributed to inhomogeneities in the ion distribution functions (*Cattell and Hudson* [1982], *Eliasson et al.* [1994]). There have been less frequent reports of sounding rocket observations of O^+ gyroharmonic structure, which is difficult to capture due to Doppler spreading (*Kintner et al.* [1989], *Bering et al.* [1975]). There have been limited reports of wave emission at the ion-ion resonant frequencies [*Lund and LaBelle*, 1997]. On the other hand, BB-ELF waves are commonly observed on both sounding rockets, and satellites [*André et al.*, 1998], and are almost always associated with TAI (*Kintner et al.* [1996],*Lynch et al.* [2002], *Knudsen et al.* [1998a]).

A statistical study carried out by *André et al.* [1998] showed that auroral field aligned currents are generally too weak to directly destabilize the CDEIC which indicated the need for additional instabilities to explain the ubiquity of BB-ELF. A leading candidate for the generation of BB-ELF are inhomogeneous electric fields (velocity shear), which have been shown to excite ion-cyclotron waves, and have been termed the inhomogenous energy density driven instability (IEDDI) [*Ganguli et al.*, 1988]. It was shown by *Gavrishchaka et al.* [2000] that

inhomogeneous parallel flow could generate ion-cyclotron waves in the auroral acceleration region. A second class of instabilities, due to inhomogeneities in the magnetic field (current shear) have been shown to destabilize ion-cyclotron waves via collisionless tearing mode instabilities, and are most recently referred to as current shear-driven instabilities (CSD) [*Seyler and Wu*, 2001]. The relationship between the fluctuating electric and magnetic fields in Alfvén waves, CSD instabilities, electron acceleration and BB-ELF plasma wave emission was made by *Seyler and Liu* [2007].

In this letter we will use observations from a multi-payload auroral sounding rocket mission to present the first direct measurement of transverse shear in the transverse flow in the topside auroral ionosphere. The directly measured shears are compared to the traditional measurement of shear and shown to be a factor of two smaller. The largest shears are measured in the regions of largest fluctuating electric fields. Associated with these fluctuating fields and shears is increased BB-ELF plasma wave emission, and narrowband wave emission at 0.9 f_{cH^+}. Coincident with these shears are regions of enhanced transverse ion acceleration (TAI).

1.3 Cascades-2 Instrumentation

The Cascades-2 sounding rocket was launched from Poker Flat Research Range (PFRR) at 11:04:00 UT on March 20th, 2009, into a pre-midnight Poleward Boundary intensification (PBI see *Mella et al.*). Early on the upleg, two Cornell Wire Boom Yo-yo (COWBOY) electric/magnetic field subpayloads with their spin axes aligned to $\mathbf{B_0}$ were ejected nearly parallel and anti-parallel to the spin axis

from the main payload with a differential velocity of 15 m/s. Each COWBOY was equipped with a pair of crossed 12.14 m dipoles formed by 4.45 cm diameter spheres deployed at the ends of coaxial wire booms. Onboard GPS receivers ensured synchronous sampling between payloads and provided positioning with $\sim$ 5 m accuracy [*Powell et al.*, 2002].

Data presented herein were taken during a 12s period on the downleg where the AFT payload traverses the altitude range from 450-433km. The payloads' GPS positions and velocities were transformed into a magnetic Vertical-East-North coordinate system, where the x-axis is aligned opposite to the local magnetic field, the z-axis points toward the magnetic North pole and y-axis completes the right handed triad. Along the magnetic field, the FWD payload was 6250-6475m above of AFT. In the plane perpendicular to $\mathbf{B}_0$, the AFT payload was 395-415m North, and 273-323m West of FWD, which formed an angle 52.5 degrees West of North that changed by less than half a degree over the selected time period. The magnitude of the inter-payload separation vector perpendicular plane, $d = |\mathbf{d}|$, went from 480m to 525m. The spacecraft velocity, v_{sc}, was 1470m/s in the plane perpendicular to $\mathbf{B}_0$ which pointed 57.3 degrees West of North.

We used a modified version of the filter/smoother described in *Humphreys et al.* [2005] to transform the raw, DC (0-1kHz), electric field data into a frame whose axes are aligned parallel and perpendicular to the projection of the inter-payload separation vector into the plane perpendicular to $\mathbf{B}_0$. The relative positions of the payloads are shown in Figure 1.1.

1.4 Cascades-2 data

Figure 1.2b shows the despun DC electric field from the FWD and AFT payloads. Figure 1.2d shows the E-field power spectrum between 20 Hz-10 kHz. Figure 1.2a shows the field aligned electron count rate from 0-1 keV (swept every 8 ms). The ”stripe” in the electron data at around 10 eV is an instrumental artifact. The fluctuating DC electric field reaches peak-to-peak values of $\sim$ 330 mV/m. Coincident with these large electric fields is a series of highly field aligned suprathermal electron bursts (STEB). Both the fields and electrons are modulated at $\sim$ 8 Hz, which is strongly indicative of Alfvénic aurora. From the lower hybrid resonance (LHR) at $\sim$ 6 kHz we obtain a rough density estimate of $1 - 2 \times 10^4$ cm^{-3}. (A more detailed density estimate will be presented later in the paper.) Magnetometer deflections of up to ~100 nt are observed indicating $|\delta E/\delta B|$ of $1 - 2 \times 10^6$ m/s which is on the order of the mass-density derived Alfvén velocity of 2.1×10^6 m/s. These magnetic field data are omitted due to our inability to achieve the sub-degree level attitude accuracy needed to accurately despin magnetometer data at these altitudes. Below f_{LH} there is evidence of increased BB-ELF activity up to ~1 kHz. Impulsive broadband features stretching from $20Hz - f_{LH}$ indicate the possible presence of Lower-Hybrid Solitary Structures (LHSS) [*Kintner et al.*, 1992].

From the despun DC electric field measurements, we can obtain the transverse plasma drift velocity, $\mathbf{V} = \mathbf{E} \times \mathbf{B}/|\mathbf{B}|^2$. To calculate shear, we approximate the spatial derivative with the finite difference $\partial V/\partial x \approx (V(x+d) - V(x))/d$, where x is the location of one payload and d is the interpayload separation distance. We assume complete field-line mapping over the $\sim$ 6.5 km parallel separation of the payloads and note that d is greater than both ion gyroradii (ρ_{O^+} = 22

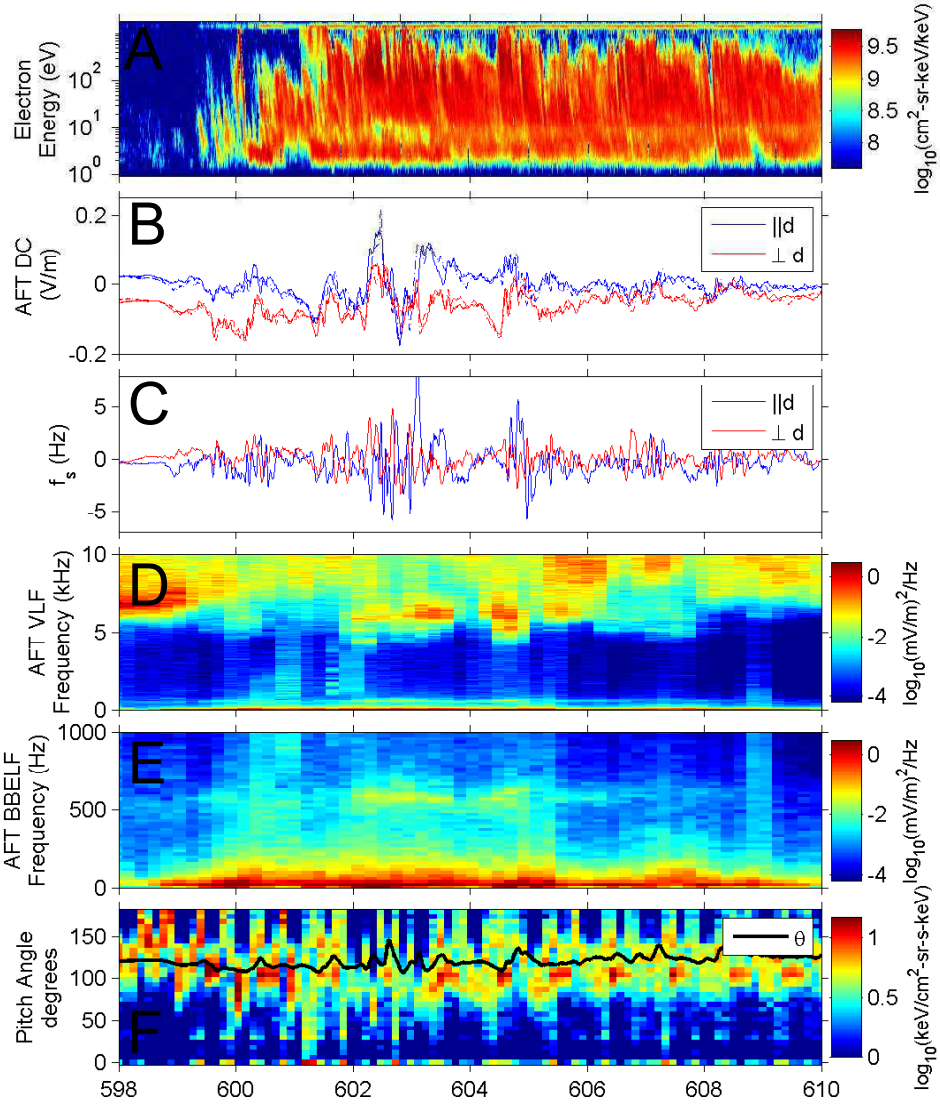

Figure 1.2: An overview of Cascades2 measurements between 598 and 610s. (A) Field aligned electrons between 0 and 1keV. (B) DC Electric field measured by the AFT payload in a coordinate system whose axes are aligned and perpendicular to the inter-payload separation vector. (C) Shear measured by differencing multipoint electric field measurements. (D) VLF plasma waves measured on the AFT payload. (E) BB-ELF plasma waves measured on the AFT payload. (F) Pitch angle energy spectrogram measured on the main payload. The black line indicates the combined payload and plasma velocity ram direction.

m,ρ_{H^+} = 1.6 m), and the electron inertial length (λ_e = 42 m). We illustrate this assumption in Figure 1.1 which shows how we are projecting the FWD payload along the nearly vertical field lines to the altitude of the AFT payload, thereby assuming all measured electric field variations are due entirely to the payloads' perpendicular separation. The choice of a separation vector aligned coordinate system allows for observation of two components of the shear, the shear in the flow parallel and perpendicular to interpayload separation vector, and is shown in Figure 1.2c. A third measurement point would allow measurement of vorticity, $\nabla \times \mathbf{V}$, which quantifies both the degree of rotation and the magnitude of shear [*Chaston et al.*, 2010]. Since our two point finite difference approximation is first order it will miss higher order spatial variations. This measurement also assumes there is no variation on scales less than the perpendicular separation of the two payloads. The highest measured shear frequency of 6Hz corresponds to velocity differences of 3000 m/s and field differences of 150 mV/m. This analysis represents a fully spatial interpretation of these signals.

Figure 1.2e displays the electric field power spectrum from 20 Hz-1 kHz from the 3-4 antenna baseline on the FWD payload. Between 20Hz and 200Hz there are increased BB-ELF emissions. In addition to enhanced BB-ELF emissions there is a narrow ($\sim$ 80 Hz wide) emission around 600 Hz. This is approximately 0.9 $\times$ f_{cH^+} where f_{cH^+} = 736 Hz (for reference f_{cO^+} = 46 Hz). These narrowband waves are highly correlated with the regions of largest shear.

Figure 1.2f shows the ion pitch angle spectrogram using energy bins from 1.5eV to 7.3eV, where 0 is aligned to $\mathbf{B}_0$. The black line in Figure 1.2f corresponds to the ram direction of the combined payload velocity and plasma drift velocity given by the expression $\theta = cos^{-1}(\mathbf{B}_0 \cdot \mathbf{v}_{rel}/(|\mathbf{B}_0||\mathbf{v}_{rel}|))$ and $\mathbf{v}_{rel} = \mathbf{v}_{sc} - \mathbf{v}_{\mathbf{E}\times\mathbf{B}}$. The

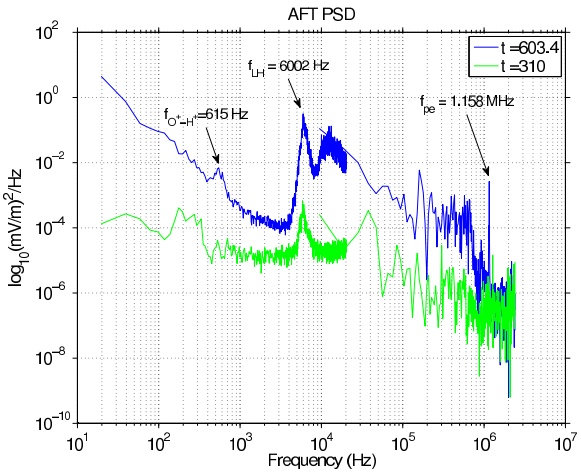

Figure 1.3: Power spectra of the VLF and HF channels indicating lower-hybrid, BB-ELF, bi-ion resonance, and langmuir waves.

majority of the ions have pitch angles within ~ 10 degrees of perpendicular. The bulk of the thermal population followed this ram direction throughout the flight; the enhancements seen during the shears, at closer to 90 deg pitch angle, may be indicative of local transverse heating. Ion temperatures during the time shown, including the times of strongest shears, were in the 1-2 eV range, hotter than in undisturbed portions of the flight (where they were often below 1 eV) but not as hot as during other arcs, where they reached up above 2 eV. Absolute temperatures of ionospheric ions, however, are as much a function of heating duration as of the strength of the heating process [*Andre and Yau*, 1997]. The thermal fluxes saturated the pitch angle imaging at the core of the distribution, so only the tail of the thermal population could be imaged. There was no mass discrimination on the ion measurements.

Figure 1.3 shows the AFT VLF and HF (1 kHz-2.4 MHz) power spectra during the active period at t=603.4 s in blue. For comparison, we include similar data from t=325s, a significantly less active period of the flight, when the payload was on the upleg and at an altitude of 518km. In the active region, we

measure a plasma frequency of 1.158MHz, which is lower than the electron cyclotron frequency f_{ce} of 1.34MHz, and therefore lower than the upper hybrid frequency. From this we determine the plasma density to be 1.34×10^4 cm^{-3}. Assuming a two component local plasma whose species are O^+ and H^+, an f_{LH} of 6002 Hz indicates a 2.5% H^+ concentration. By repeating this analysis for a number of cases on both payloads and at numerous times we find the H^+ concentration to be between 2-3% for the entire region of narrowband wave emission. The existence of a second ionic component introduces two new frequencies of interest, the bi-ion resonance and cutoff frequencies [*Buchsbaum*, 1960]. For a 2.5% H^+, 97.5% O^+ plasma, the bi-ion resonance frequency is 615Hz [*Smith and Brice*, 1964]. In addition to the EIC modes and the bi-ion resonances, the other electrostatic plasma wave mode below f_{LH} is the ion-acoustic mode, which is less likely to be unstable in the topside auroral ionosphere [*Kindel and Kennel*, 1971]. An alternative interpretation of these narrowband waves is that they are spatial structures of 2.4 m Doppler shifted by the ~1500 m/s spacecraft velocity perpendicular to the magnetic field ($2\pi f_{doppler} = v_\perp^{s/c}$ k).

1.5 Discussion

The choice of separation vector aligned coordinate system and the near collinearity of the d and $v_\perp^{s/c}$ allows for a comparison between traditional methods of measuring shear. We apply the traditional measurement of shear (e.g. *Kelley and Carlson* [1977], *Earle et al.* [1989]) to our largest peak-to-peak DC electric field variation. This variation of 336mV/m, in the direction aligned to the interpayload separation vector, was recorded over .43s at 602s into the flight, while the velocity of the payload perpendicular to $\mathbf{B_0}$ was ~1500 m/s. From these parame-

ters we obtain a shear frequency estimate of ~12Hz. This is significantly higher than our directly measured shears indicating that a significant portion of the measured electric field fluctuations must be temporal, i.e., the slope in the measured electric field is due both to the spacecraft's motion through a structured electric field and that structured field's dynamic evolution and propagation past the spacecraft. In both directions the shear is both positive and negative, indicating passage through spatially oscillatory structures.

Ganguli et al. [1994] outline a hierarchy of micro-instabilities that can be triggered by velocity shear. Our measured shear frequency of $\sim .125\Omega_{cO^+}$ falls between the IEDDI case, where $\omega_s \sim \omega_{Ci}$, and the Kelvin-Helmholtz (KH) instability case, where $\omega_s \ll \omega_{Ci}$. IEDDI mechanisms have been shown to produce EIC type waves which are broadband [*Ganguli et al.*, 1994]. In general, the response of the plasma is to dissipate shears, so although we observe shear frequencies below the IEDDI excitation threshhold, there could be shears above it prior to our measurement time [*Romero and Ganguli*, 1993]. In certain cases, simulation has shown that the non-linear evolution and steepening of the KH instability can develop small scale regions of intense shear which can then excite IEDDI [*Ganguli et al.*, 1994]. The general IEDDI theory has been extended to multi-component plasmas and it has been shown that this destabilizes plasma waves at 0.9-0.95 times the minority species cyclotron frequency [*Gavrishchaka et al.*, 1997], strongly suggesting our observed narrowband plasma waves are IEDDI driven.

In the CSD instabilities of *Liu et al.* [2006], regions of largest current shear correspond to regions of largest DC electric field. Because our measured regions of highest shear are collocated with the most intense DC electric fields, we can-

not discount CSD mechanisms. We illustrate the difficulty of distinguishing between the IEDDI and CSD modes with a simple example. Imagine a 1 Hz, inertial Alfvén wave with a perpendicular wavelength of 1000m, detected by measuring a δE of 100 mV/m. On scales of 500m, shear frequencies of up to 10 Hz would be measured, and exist, in the region between the peak and trough of this wave. The growth rate of the IEDDI in this situation would be on the order of $0.01 - 0.05\Omega_{O^+}^{-1}$, which is close to the 1s period of the Alfvén wave, and would therefore be slightly unstable. Following the inertial Alfvén wave dispersion relation, $|\frac{\delta E}{\delta B}| = V_a\sqrt{1 + k_\perp^2\lambda_e^2}$, δB in this scenario would be 50 nT. Since there is no excitation threshold for CSD, the very existence of an Alfvén aurora is sufficient to destabilize it. Given its lack of excitation threshold, we believe the CSD instability is a more likely candidate to explain the observed BB-ELF. This may explain why we observe BB-ELF waves over the entire active region rather than just the region of highest shears. However, given the complexity of Alfvénic aurora, either the CSD or the IEDDI could be significant, and we believe the best explanation for the observed BB-ELF may be a combination of both.

In conclusion, we present the first direct measurement of velocity shear in the topside auroral ionosphere above an active auroral display, and measure shear frequencies in excess of 6Hz. This directly measured shear is a factor of two less than traditional measurement techniques would imply applied to the same data set, indicating the need to consider propagation effects when interpreting DC electric field structures. We do not attempt to explain the mechanism that supports these differences and instead focus on the microphysics driven by them. These shears were measured in regions of intense, fluctuating DC electric fields. High shear regions ($f_s > 4$) are collocated with BB-ELF plasma waves, and narrowband low frequency plasma waves occurring at the bi-ion resonance

frequency. The existence of these narrowband waves are highly likely due to the IEDDI. The plasma wave data implies the existence of minority ionic constituent indicating the need to include them in future simulation and modeling work.

CHAPTER 2

MULTI-PAYLOAD INTERFEROMETRIC WAVEVECTOR DETERMINATION OF AURORAL HISS

2.1 Abstract

We extend traditional, single payload, interferometric techniques to a multiple payload sounding rocket mission, and apply these techniques to measure the parallel and perpendicular wavelength of auroral VLF hiss from 8kHz-20kHz. We model the wavelength distribution of auroral hiss as a cone at a fixed angle with respect to the magnetic field that is isotropically distributed in the perpendicular plane. We apply this model to calculate the interferometric observables, coherency and phase, for a sounding rocket mission whose wave electric field receivers are on payloads that are separated 2-3km along the magnetic field and 55-200m across the magnetic field. Using an interferometer formed by comparing the collinear sphere-to-skin electric field antennas on a single payload, we estimate a lower limit on the perpendicular wavelength of VLF hiss of $\sim$ 60m. Analysis of coherency and phase due to this conical wave-vector distribution for a multi-payload interferometer reveals the existence of a spin dependent coherency pattern. From this coherency pattern we generate an upper limit perpendicular wavelength estimate for VLF hiss of $\sim$ 350m. The inter-payload phase gives an accurate estimate of the parallel wavelength of $\sim 6000 - 8000$m. This parallel wavelength is combined with the lower (upper) limit perpendicular wavelength estimates to generate upper (lower) limits on wave-normal angle. These limits are each within one degree of the predicted electrostatic whistler wave resonance cone angle verifying that VLF hiss propagates on this

resonance cone.

2.2 Introduction

Due to its generation via electron precipitation auroral hiss is a ubiquitous feature of the auroral ionosphere [*Maggs*, 1976]. Auroral hiss is a whistler mode plasma wave radiation that propagates in a band between the lower hybrid frequency, f_{LH}, and either the local plasma frequency, f_{pe}, or the local electron cyclotron frequency,f_{ce}, whichever is lower. The observation of enhanced wave power at f_{LH} is due to linear mode conversion from the long wavelength, propagating VLF hiss to shorter wavelength lower-hybrid waves near the lower hybrid resonance (LHR). A review of space and ground observation of auroral hiss along with applicable plasma wave theory is given by *LaBelle and Treumann* [2002].

From *in-situ* electric and magnetic field observations, *Gurnett and Frank* [1972] identified two types whistler mode wave patterns, VLF saucers and VLF hiss. VLF saucers are identified by a characteristic "saucer" shape in frequency-time spectrograms dependent on the satellite's position relative to the saucer source region. The characteristic shape is due to relatively small source regions, which can be viewed as point emitters, and the whistler waves' frequency dependent group velocity. VLF hiss, on the other hand, is generally broad-band, has a larger source region and has a Poynting vector aligned down the magnetic field.

Sounding rocket studies have been important for studying the transition from whistler mode waves to electrostatic lower hybrid waves. *Ergun et al.* [1991] used a quadrupole VLF wave receiver to measure perpendicular wave-

lengths of ~12m near f_{LH} at ~4kHz and up to ~70m at 10kHz. These results were confirmed and extended by *Kintner et al.* [2000] who used interferometric techniques to determine that the perpendicular wavelength of VLF hiss was at least ~80m at 20Khz. Due to its connection to lower hybrid waves VLF hiss is an energy source for lower hybrid solitary structures (LHSS) [*Schuck et al.*, 2003]. LHSS are gyro-scale, ~ 40m wide, cylindrical, 10−50% density depletions. These density depletions may be formed and sustained by VLF hiss and lower hybrid waves scattering off of pre-existing plasma density irregularities.

The promise of spaced measurements in space plasma is a resolution to the spatio/temporal ambiguity that plagues single point measurements. The introduction of multiple satellite missions such as CLUSTER, and multi-point measurements from a single platform on both satellites and rockets has yielded a number of techniques to solve this ambiguity. The most common technique at VLF frequencies is interferometry [*Kintner et al.*, 2000]. Two competing techniques have arisen for analysis of low frequency (DC-2Hz) plasma waves from multiple satellites; k-filtering and phase differences. The k-filtering technique (also known as the wave telescope) applies a filter bank to all available baselines which estimates the spectral power at a given wave number in a maximum likelihood sense [*Pincon and Lefeuvre*, 1992]. The phase differences method deduces the wave vector by using wavelet based interferometry to measure the phase between many different baselines [*Dudok de Wit et al.*, 1995a].

Using spaced *in-situ* plasma wave receivers we are able to directly measure the parallel wavelength for the first time, and bound the perpendicular wavelength of auroral hiss. Within these bounds we show that VLF hiss lies on the whistler wave resonance cone. This paper is organized in 5 sections. First we

introduce the Cascades2 sounding rocket. Second we review traditional plasma wave interferometric techniques and extend them for our multi-payload sounding rocket mission. Third we present the multi-payload interferometry observations. Fourth we present a discussion of the observations. In the last section we draw conclusions.

2.3 Experimental Setup

The Cascades2 sounding rocket was launched at 11:04:00 UT on 20, March 2009 from Poker Flat Research Range outside of Fairbanks, Alaska. After powered flight, two Cornell wire-boom electric/magnetic field sub-payloads were ejected from a main payload at high velocity, 15 m/s, along their spin axes which were aligned to local magnetic field, $\mathbf{B}_0$. Onboard GPS receivers provided absolute and relative position to the ~5m level and relative timing to the ~175ns level [*Powell et al.*, 2002]. Each payload was equipped with a pair of crossed 12.14m dipole antennas formed by 4.45cm diameter spheres at the ends of coaxial wire booms. These four spheres and the payload skin formed 6 antennas on each payload: 2 formed by the crossed dipoles, and 4 formed by measuring the potential difference between each individual sphere and the payload skin. Each antenna was connected to at least two plasma wave receivers, one measuring from DC to 1kHz, and one measuring from 20Hz to 20kHz. One sphere pair on each payload was equipped with an HF snapshot receiver that took 4096 samples at 4.8MHz (8.53 μ s of data) once every 10ms. All data presented were taken with the VLF (20Hz-20kHz) plasma wave receivers. Antenna orientation was deduced post flight from a modified version of the attitude determination filter/smoother presented in *Humphreys et al.* [2005].

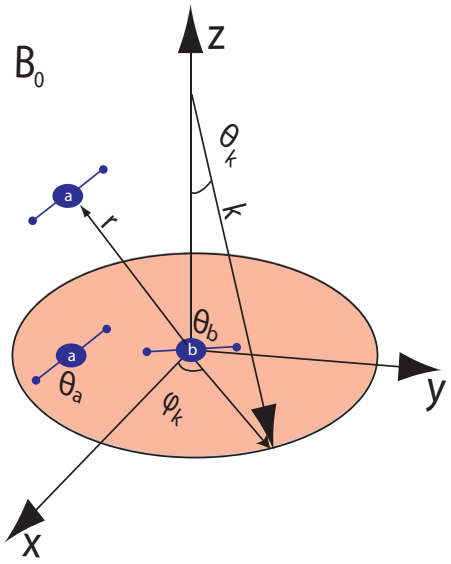

Figure 2.1: A diagram describing the relative positions and orientations of the payloads and the wave-vector distribution. (Not to scale.)

Data presented herein were taken from 350-450s flight time as the payload array approached and passed its ~ 562km apogee, which occurred 430s into the flight. Payload positions were transformed into a magnetic Vertical, East, North coordinate system where the x-axis is anti-aligned to the geomagnetic field, the z-axis points to the magnetic pole and the y-axis completes the right handed triad. During this 150s time period, payload *a* went from 2500m to 4250m in front of payload *b*, along the magnetic field. In the perpendicular plane, payload *a* began 20m to the North of payload *b*, before payload *b* passed it at 379s. By 500s payload *a* was 170m South of payload *b*. Payload *a* went from 40 to 158m East of payload *b*. Figure 2.1 displays a cartoon of the relative payload positions, and panels A and B of Figure 2.5 show the relative payload position in the perpendicular plane and along the magnetic field, respectively. These relative motions are due to the payloads' differing orbits and the curvature of $\mathbf{B}_0$.

Due to slight differences in inertia properties, the sub-payloads had slightly different spin rates such that payload *a* completed one extra revolution over the course of the ~750s flight. Over this time period the payloads' velocity was ~1780m/s pointing ~62 degrees West of North in the plane perpendicular to $\mathbf{B}_0$. The relative positions and orientations of the payloads are sketched in Figure 2.1. Electron data were taken on the main payload which was situated between the two wire-boom payloads.

2.4 Interferometry

We begin our derivation of the coherency and phase response of the Cascades2 interferometers with a discussion of the response of a dipole antenna to an electrostatic plane wave. The dipole antenna measures the potential difference between two points in space where those points are either the electrically coupled spheres at the ends of the wire-booms or the payload's aluminium body. We convert this voltage into an electric field by dividing by the distance between the two measurement points. We consider the frequency domain representation of the electric field due to a plane wave of frequency ω, wavevector $\mathbf{k}$, and phase ϕ, $\mathbf{E}(\mathbf{x}, t) = E_0\hat{\mathbf{k}}\exp(i(\mathbf{k}\cdot\mathbf{x}+\omega t+\phi))$. The voltage measured between two points due to this wave is given by the integral form of Faraday's law, $V_{12} = \int_{\mathbf{X}_2}^{\mathbf{X}_1} \mathbf{E}\cdot\mathrm{d}\mathbf{l}$. The position and orientation of the antenna are defined by $\mathbf{r}$ and $\mathbf{d}$, where $\mathbf{r} = (\mathbf{x}_2+\mathbf{x}_1)/2$ and $\mathbf{d} = (\mathbf{x}_2 - \mathbf{x}_1)$. The antenna response, $s = V_{12}/|d|$, and its Fourier transform are given by Equations 2.1 and 2.2, respectively.

$$s(\mathbf{r}, \mathbf{d}) \quad = \quad E_0\hat{\mathbf{k}}\cdot\hat{\mathbf{d}}\,\mathrm{sinc}(\mathbf{k}\cdot\mathbf{d}/2)\exp(i(\omega t + \mathbf{k}\cdot\mathbf{r} + \phi)) \tag{2.1}$$

$$\hat{s}(\omega) \quad = \quad E_0 \hat{\mathbf{k}} \cdot \hat{\mathbf{d}} \, \mathrm{sinc}(\mathbf{k} \cdot \mathbf{d}/2) \exp(i(\mathbf{k} \cdot \mathbf{r} + \phi)) \delta(\omega - \omega_k) \tag{2.2}$$

Equation 2.1 has three main features. First is the $\hat{\mathbf{k}} \cdot \hat{\mathbf{d}}$ term which defines the relative wavevector/antenna orientation dependence. Second is the $\mathrm{sinc}(\mathbf{k} \cdot \mathbf{d}/2)$ term which describes the antenna attenuation at wavelengths shorter than the antenna (note that $\mathrm{sinc}(x) = \sin(x)/x$). And third is the $\exp(i(\mathbf{k} \cdot \mathbf{r} + \omega t + \phi))$ term which models the propagation of the wave past the antenna. The dirac delta in Equation 2.2 is due to the Fourier transform, and is dropped for the remainder of the article since the frequencies and wavelengths of interest aren't affected by doppler shift. Equation 2.1 is easily extended to wave distributions via integration or summation over a distribution.

The interferometric observables, which were first introduced in the radar community by *Farley et al.* [1981], are coherency,γ^2, and phase, ψ, and are constructed from a generalized spectral product P_{ab}. This spectral product is defined as $\mathrm{P}_{ab}(\omega) = \langle \hat{s}_a(\omega) \hat{s}_b(\omega) \rangle$, where $\hat{s}_a$ and $\hat{s}_b$ are fourier transforms of signals s_a and s_b and the braces denote an ensemble average. In practice s_a and s_b are discretely sampled time series and $\hat{s}_a$ and $\hat{s}_b$ are calculated via the fast fourier transform (FFT). Following *Bonnell* [1997] the squared coherency and phase are defined in equations 2.3 and 2.4 respectively. We neglect the effect of noise in the measurements as it was shown by *Kintner et al.* [2000] to slightly decrease the measured coherency.

$$\gamma^2(\omega) = \frac{\mathrm{P}_{ab}(\omega)\mathrm{P}_{ab}(\omega)^*}{\mathrm{P}_{aa}(\omega)\mathrm{P}_{bb}(\omega)} \tag{2.3}$$

$$\psi(\omega) = \tan^{-1}(\Im(P_{ab}(\omega))/\Re(P_{ab}(\omega))) \tag{2.4}$$

The general expression for the cross-spectral product for a distribution of plane waves is given by Equation 2.5 which places antennas a and b at positions $\mathbf{r}_a$ and $\mathbf{r}_b$, with orientations $\mathbf{d}_a$ and $\mathbf{d}_b$ and allows for arbitrary phases p and q between each realization.

$$\begin{aligned} \mathrm{P}_{ab} &= \langle \int_{\mathbf{k}_p} E_0 \hat{\mathbf{k}_p} \cdot \hat{\mathbf{d}}_a \mathrm{sinc}(\mathbf{k}_p \cdot \mathbf{d}_a/2) \exp(i(\mathbf{k}_p \cdot \mathbf{r}_a + \phi_p)) \mathrm{d}\mathbf{k}_p \\ &\quad \int_{\mathbf{k}_q} E_0 \hat{\mathbf{k}_q} \cdot \hat{\mathbf{d}}_b \mathrm{sinc}(\mathbf{k}_q \cdot \mathbf{d}_b/2) \exp(-i(\mathbf{k}_q \cdot \mathbf{r}_b + \phi_q)) \mathrm{d}\mathbf{k}_q \rangle \end{aligned} \tag{2.5}$$

We model the quasi-electrostatic VLF-hiss waves as a cone in wave vector space as shown in Figure 2.1. This cone is defined by a single wavenumber k at a fixed zenith angle θ_k with respect to $\mathbf{B}_0$, an azimuthal angle φ_k and a random phase such that $\mathbf{k} = k[\sin(\theta_k)\cos(\varphi_k), \sin(\theta_k)\sin(\varphi_k), \cos(\theta_k)] = [k_\perp \cos(\varphi_k), k_\perp \sin(\varphi_k), k_\parallel]$. The random phase imposes a filter condition inside the expectation which reduces the summation over a double integral in Equation 2.5 to a single integral over $\mathbf{k}$ as shown in equation 2.6.

$$\begin{aligned} \mathrm{P}_{ab} &= E_0^2 \int_{\mathbf{k}} (\hat{\mathbf{k}} \cdot \hat{\mathbf{d}}_a)(\hat{\mathbf{k}} \cdot \hat{\mathbf{d}}_b) \mathrm{sinc}(\mathbf{k} \cdot \mathbf{d}_a/2) \mathrm{sinc}(\mathbf{k} \cdot \mathbf{d}_b/2) \\ &\quad \exp(i(\mathbf{k} \cdot (\mathbf{r}_a - \mathbf{r}_b))) \mathrm{d}\mathbf{k} \end{aligned} \tag{2.6}$$

The Cascades2 experiment has a number of VLF wave antennas/recievers with which to construct interferometers. We begin our investigation of Equation 2.6 by calculating the power spectral density, P_{aa}, which will be similar for all antennas due to their orientation perpendicular to $\mathbf{B}_0$. The antennas' orientation perpendicular to $\mathbf{B}_0$ reduces the integral over $\mathbf{k}$ to an integral over φ_k. Since $\mathbf{k}$ is isotropically distributed in the plane perpendicular to $\mathbf{B}_0$ we can arbitrarily

align $\mathbf{d}_a$ along the x-axis without loss of generality. Equation 2.6 becomes

$$\begin{aligned} \mathrm{P}_{aa} &= \left|\frac{2E_0}{kd}\right|^2 \int_0^{2\pi} \sin^2\left(\frac{kd}{2}\cos(\varphi_k)\right)\mathrm{d}\varphi_k \\ &= \left(\frac{2E_0}{kd}\right)^2 \pi(1 - J_0(kd)) \end{aligned} \tag{2.7}$$

where J_0 is the Bessel function of the first kind of order zero.

As mentioned above, each payload has six VLF wave antennas, the two crossed dipoles and each individual sphere to the payload skin. We calculate P_{ab} for two of the possible single payload interferometers: 1) collinear sphere-to-skin channels, and 2) the crossed dipoles. The coherency response for an interferometer formed by comparing collinear sphere-to-skin antennas was originally calculated numerically by *Kintner et al.* [2000]. We simplify Equation 2.6 for this interferometer by aligning it along the x-axis such that $\mathbf{d}_a = \mathbf{d}_b = [d; 0; 0]$ and $\mathbf{r}_a = [r; 0; 0]$, $\mathbf{r}_b = [0; 0; 0]$ which is solved analytically. The cross spectral product is then given by

$$\begin{aligned} P_{ab} &= E_0^2\left(\frac{2}{kd}\right)^2 \int_0^{2\pi} \sin^2(kd/2\cos(\varphi_k))\exp(ikr\cos(\varphi_k))\mathrm{d}\varphi_k \\ &= \frac{2\pi E_0^2}{(kd)^2}(2J_0(kr) - J_0(k(r-d)) - J_0(k(d+r))). \end{aligned} \tag{2.8}$$

To calculate coherency for this single payload interferometer we insert equations 2.8 and 2.7 into 2.3

$$\gamma^2 = \frac{(2J_0(kr) - J_0(k(r-d)) - J_0(k(d+r)))^2}{4(1 - J_0(kd))^2}. \tag{2.9}$$

Equation 2.8 is always real which means that the phase for this interferometer is always equal to zero as was shown in *Kintner et al.* [2000]. We plot this coherency as a function of antenna length and antenna separation in Figure 2.2.

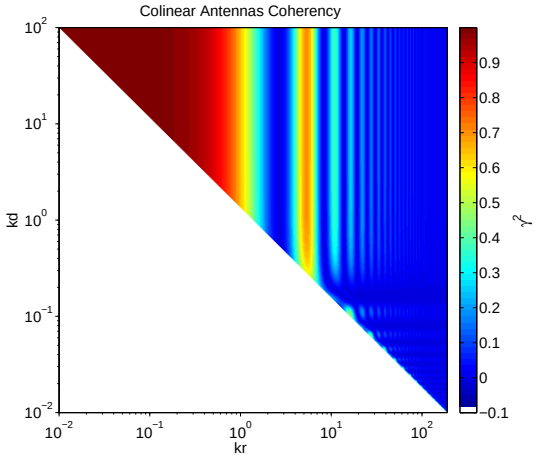

Figure 2.2: Coherency as a function of antenna length (y-axis) and antenna separation (x-axis) for a distribution of planes wave isotropically distributed in the plane perpendicular to $\mathbf{B}_0$. The white area is where the antenna length is longer than the separation between antennas which isn't physically realizable.

Coherency near unity occurs for perpendicular wavelengths much longer than the antenna separation. An interference pattern occurs for shorter wavelengths with the first null occurring at $J_0(kr) = 0$, $kr \simeq 2.404, \lambda = 2.612r$. We omit coherency calculation for $d >= r$ as this geometry hasn't been realized in sounding rocket applications. An approach for wavelength estimation from two collocated antennas of different lengths is presented in *Kelley and Mozer* [1972].

A second single payload interferometer can be made by comparing signals from the crossed dipoles. In this case we align antenna a along the x-axis and antenna b along the y-axis such that $\mathbf{d}_a = [d; 0; 0], \mathbf{d}_b = [0; d; 0]$. The cross-spectral product becomes

$$\begin{aligned} \mathrm{P}_{ab} &= \left(\frac{2E_0}{kd}\right)^2 \int_0^{2\pi} \sin\left(\frac{k_\perp d\cos(\varphi_k)}{2}\right)\sin\left(\frac{k_\perp d\sin(\varphi_k)}{2}\right)\mathrm{d}\varphi_k \\ &= 0. \end{aligned} \tag{2.10}$$

This cross-spectral product of 0 leads to a straight forward interpretation of the

coherency of 0. In theory we cannot calculate the phase for this interferometer due to the division operation in Equation 2.4. In practice measurement noise will always give P_{ab} a finite length in the complex plane which leads to a measured phase.

For multi-payload interferometers, arbitrary antenna orientations complicate the integral in Equation 2.6 by introducing an absolute orientation dependence, i.e., the cross spectral product depends on the antenna orientations with respect to each other and with respect to the inter-payload separation vector. To simplify, we place payload b at the origin and define payload a's position in cartesian coordinates, $\mathbf{r}_b = \left[r_x; r_y; r_\parallel\right]$. The antenna orientations in the plane perpendicular to $\mathbf{B}_0$ are defined by the angles θ_a and θ_b measured from the x-axis. The expression for the cross-spectral product becomes

$$\begin{aligned} P_{ab} &= \frac{4E_0^2}{|k|^2|d|^2}\exp(ik_\parallel r_\parallel) * \\ &\quad \int_0^{2\pi} \sin(\mathbf{k}\cdot\mathbf{d}_a/2)\sin(\mathbf{k}\cdot\mathbf{d}_b/2) * \\ &\quad \exp(ik_\perp(r_x\cos(\varphi_k) + r_y\sin(\varphi_k)))\mathrm{d}\varphi_k. \end{aligned} \tag{2.11}$$

By utilizing sum-to-product trigonometric identities in the antenna orientation terms, $\mathbf{k}\cdot\mathbf{d}_{a,b}$, can be rewritten as $k_\perp d\cos(\varphi_k - \theta_{a,b})$, which makes their φ_k dependence explicit. The evaluation of this integral is complicated by these sine of cosine terms along with the existence of both $\sin(\varphi_k)$ and $\cos(\varphi_k)$ in the complex exponential.

The integral in Equation 2.11 is sufficiently complicated that we resort to computing it numerically. The first observation is that the integrand in Equation 2.11 is always real which means that the only contribution to the inter-

payload phase comes from the exp($ik_{\parallel}r_{\parallel}$) term. When calculating the coherency, γ^2, this term gets multiplied by its conjugate which removes all $r_{\parallel}$ and $k_{\parallel}$ dependence. The coherency is then a function of the relative antenna orientations and their perpendicular separation. Panels A,B and C of Figure 2.3 displays this coherency pattern for three different relative antenna angles, $\theta_b = 0.0, \pi/4, \pi/2$ while holding $\theta_a = 0$. Panels D, E and F of Figure 2.3 show the relative antenna orientation for the coherency patterns displayed in panels A,B and C, respectively. We've fixed payload b at the origin, so panels A, B and C of Figure 2.3 display the coherency that would be measured between two payloads for a second payload at position $[r_x, r_y]$ where r_x and r_y are denoted by the x and y axes of each plot. The essence of this calculation is that we will observe enhanced coherency in regions of space where both antennas detect waves. Since we've fixed θ_a these plots represent snapshots of the spatial coherency pattern for Cascades2. As the payloads spin the location of the second payload will describe a circle with nearly fixed radius around the origin. This will produce a pattern of nulls in the coherency spectrum. Since the payloads aren't rotating at the same rate the coherency and null pattern will change as a function of time.

2.5 Data Presentation

Panel A of Figure 2.4 displays the power spectral density from the FWD payload (payload a in Figure 2.1) between 20Hz-20kHz. Panel B of Figure 2.4 displays electron count rate between 0-1keV from a high time resolution electron detector on the main payload. The VLF wave power is concentrated near the lower hybrid frequency, f_{LH}, of $\sim$ 5kHz. Below f_{LH} there exist broadband, impulsive features that have been identified as lower hybrid solitary structures (LHSS)

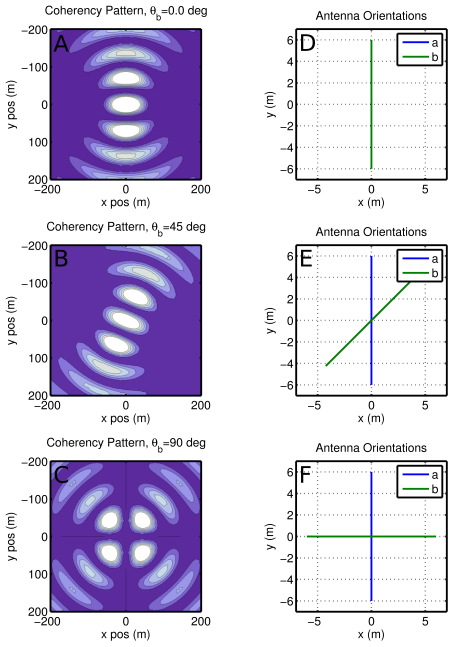

Figure 2.3: Coherency pattern in the plane perpendicular to $\mathbf{B}_0$ for different antenna orientations. The left column (panels A, B and C) show the coherency as a function of the the interpayload separation distance for the relative antenna orientation in the right column (panels D, E and F).

from 385s to 475s. Consistent with the model of VLF hiss as a whistler-mode radiation generated by precipitating auroral electrons that has propagated a long distance from its source, the majority of the VLF wave power exists outside of regions of active auroral electron precipitation, which occur for 10s around 425s and from 475s on.

The inter-payload coherency and phase are displayed in panels B and C of Figure 2.5 respectively. Panel A of Figure 2.5 shows the inter-payload separation distance in the plane perpendicular to $\mathbf{B}_0$. Panel 4 shows the separation distance parallel to $\mathbf{B}_0$ on the right axis, and the angle between the inter-payload separation vector and the IGRF derived $\mathbf{B}_0$ on the left axis. The white line in panel

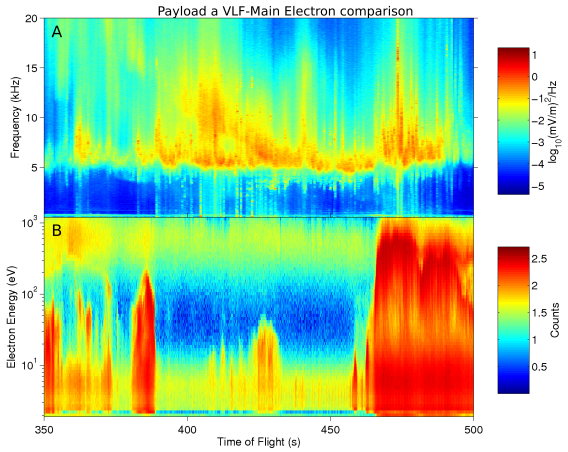

Figure 2.4: Overview of Cascades2 VLF wave and electron data. (A) VLF wave power spectrum from payload a. (B) Pitch angle integrated electron count rate from the Main Payload.

C is the root-mean-square (RMS) perpendicular separation and corresponds to the right axis.

While the payloads are closely aligned along the magnetic field, and while there exists significant wave power we observe interpayload coherency near unity. As the payloads separate across the magnetic field, as a consequence of both the changing magnetic dip angle and the payloads differing orbits, the coherency decreases. Where there are coherent emissions the inter-payload phase is quite uniform changing from ~ 150 degrees at 375s to ~ 180 degrees at 450s. Note that the timing delay between payloads is at most 175ns which would introduce a 2 degree error in the interpayload phase.

We restrict our investigation of VLF hiss to the period between 375s and 385s because this period is relatively free of LHSS and is far from the auroral electron beam, both of which could alter the validity of our wave-vector distribution model. Following *Kintner et al.* [2000] we calculate the coherency and phase for a interferometer formed by collinear sphere-to-skin channels on a single pay-

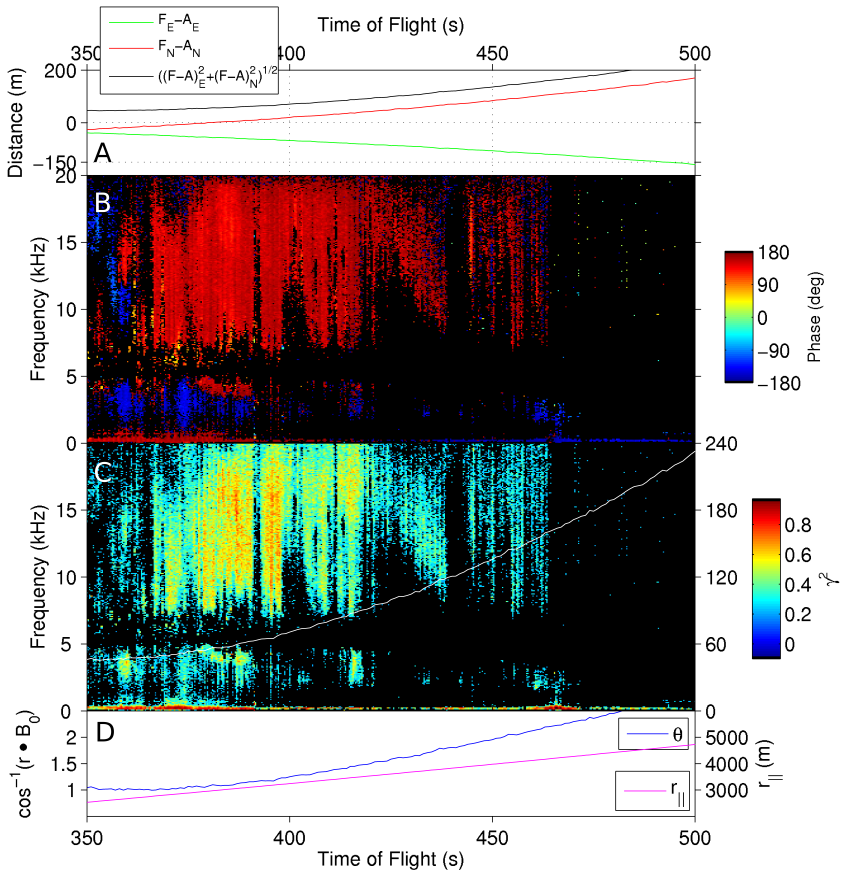

Figure 2.5: (A) Separation between payloads *a* and *b* in the plane perpendicular to $\mathbf{B}_0$. (B) Interpayload phase; (C) interpayload coherency and RMS perpendicular separation (white line and right axis). (D) The angle between the interpayload separation vector and $\mathbf{B}_0$ (left axis) and the separation between payloads *a* and *b* parallel to $\mathbf{B}_0$.

load. Figure 2.6 displays the coherency (panel A) and phase (panel B) for the AFT payload (payload *b* in Figure2.1). From ~ 1.5 – 2kHz above f_{LH} and higher the coherency is always between 0.95 and 1.0 and the phase is always within a few degrees of 0.0, indicating perpendicular wavelengths at least 10 times our antenna separation distance of 6m isotropically distributed in the plane perpendicular to $\mathbf{B}_0$. The low coherency for the ~ 1.5 – 2kHz above f_{LH} indicates that these lower-hybrid waves have wavelengths less than the interferometer length of 6m.

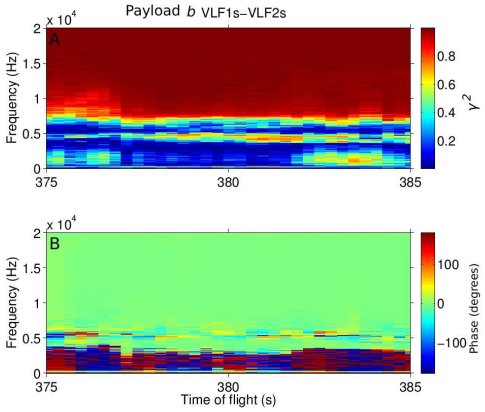

Figure 2.6: Coherency (A); and phase (B); from collinear sphere-to-skin channels on payload *b*.

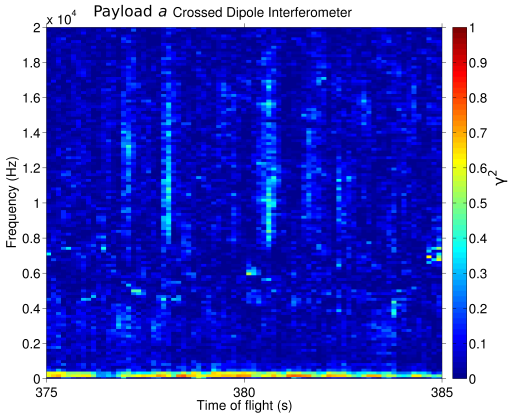

Figure 2.7: Coherency for the crossed dipole interferometer from payload *a*.

We construct a second single payload interferometer comparing signals measured from the crossed-dipole channels on the FWD payload. The coherency for this interferometer is plotted in Figure 2.7 and is nearly always 0.0 and is always below 0.3 for frequencies above f_{LH}. The coherent emissions below f_{LH} are due to a different wave mode and will be discussed in a future publication. The calculations leading to Figures 2.6 and 2.7 have been repeated for all similar interferometry baselines available and returned similar results.

Panel B of Figure 2.8 displays the coherency measured between the payloads. During this 10s period of the flight payload *a* is ~ 3000m ahead of *b* parallel to $\mathbf{B}_0$, and the payloads are separated ~ 55m in the perpendicular plane as is displayed in the top panel of 2.8. The altitude of the payload *b* is ~ 550km Panel C displays the absolute orientation of antenna *a* with respect to the projection of the inter-payload separation vector into the plane perpendicular to $\mathbf{B}_0$ indicating the payloads undergo ~ 4 revolutions. Panel D displays the relative antenna orientation between the two payloads measured from payload *a*. The vertical black lines identify nulls in the coherency spectrum and are used in the forthcoming discussion.

2.6 Analysis and Discussion

There are three sources of information about the perpendicular wavelength: (1) the collinear antennas on a single payload, (2) the location and depth of the nulls in the inter-payload coherency calculation, and (3) the decrease in coherency as the payloads separate across the magnetic field. As mentioned previously, the high coherency observed between two collinear antennas on a single payload (Figure 2.2) indicates perpendicular wavelengths at least 10 times the 6m interferometer length.

During the 10s period displayed in Figure 2.8 the relative orientation of the antennas changes by ~ 8 degrees, from -45 degrees to -53 degrees. This slight change doesn't significantly affect the coherency pattern. Figure 2.9 displays the theoretical coherency pattern as a function of spin for this multiple payload interferometer. The vertical lines in Figure 2.9 are chosen to match those of

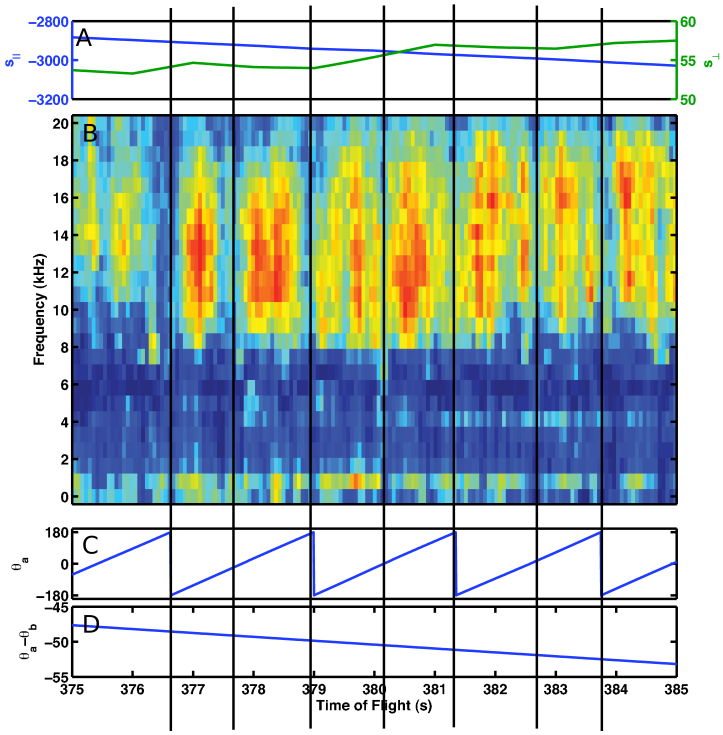

Figure 2.8: (A) Distance between a and b in the planes parallel (left axis) and perpendicular (right axis) to $\mathbf{B}_0$. (B) The interpayload coherency. (C) The absolute orientation of antenna a with respect to the interpayload separation vector. (D) The relative orientation of antenna b with respect to antenna a. The vertical lines identify nulls in the coherency spectrum.

Figure 2.8. From the spin dependence and shallow depth of the nulls in Figure 2.8 we determine and upper limit of the perpendicular wavelength at $kr = 1.$, or $\lambda = 450m$.

The decrease in measured coherency as a function of increasing inter-payload separation distance displayed in Figure 2.5 provides an *ad-hoc* estimate of the perpendicular wavelength. In the interpayload coherency patterns displayed in Figure 2.3 a null always occurs at $2.612 * r = \lambda$. We could then interpret the disappearance of coherent emission at 475s as entry into this null leading to a

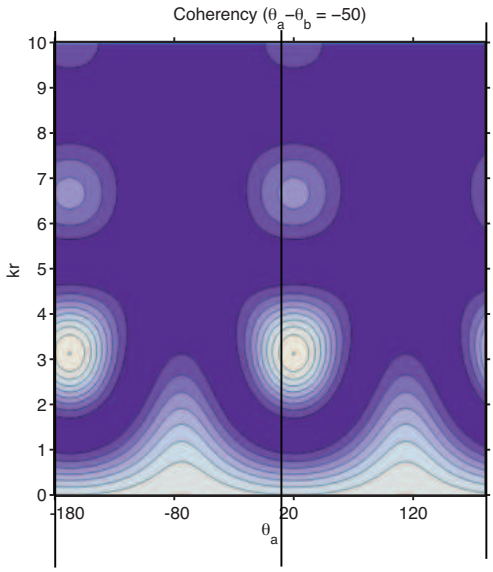

Figure 2.9: Coherency as a function of spin for a dual payload interferometer whose relative spin angle is -50 degrees. The x-axis, θ_a, is the orientation of payload a with respect to the inter-payload separation vector.

perpendicular wavelength estimate of $\lambda = 266m$.

Since the interpayload phase is entirely due to payloads' parallel separation, ie, $k_{\|}r_{\|} = \psi + 2\pi n$ radians where $n = 0, 1, 2, 3, ...$, we can use the inter-payload phase to estimate parallel wavelength. We assume $n = 0$, and solve the expression relating $k_{\|}$ and ψ for the parallel wavelength, which is plotted as a function of frequency in panel A of Figure 2.10. There is some evidence of phase wrap-around after ~450s which occurs when the inter-payload separation distance, $r_{\|}$, is equal to an integer number of half wavelengths.

From the cold, two fluid plasma dispersion relation, *Maggs* [1976] derives an expression for the resonance cone-angle for VLF-hiss, $\phi_r = \tan^{-1}(k_{\perp}/k_{\|})$. (Note that the angle ϕ_r is the angle between $\mathbf{k}$ and $\mathbf{B}_0$.) The resonance cone angle is given by Equation 2.12, where R= ω_{pe}/Ω_{ce} is the ratio of the plasma frequency

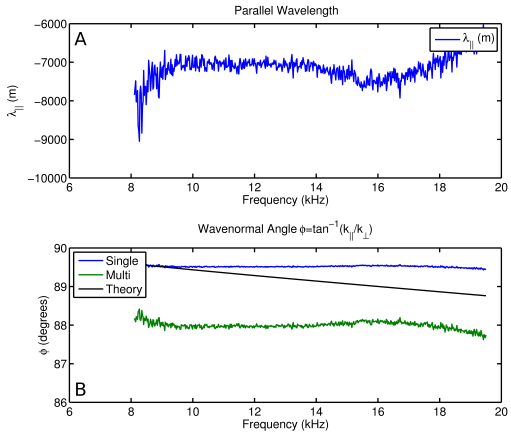

Figure 2.10: (A) The parallel wavelength deduced from inter-payload phase. (B) The wave-normal angle.

to the electron cyclotron frequency, z= ω/Ω_{ce} is the ratio of the wave frequency to the electron cyclotron frequency, and ξ is the electron to ion mass ratio. We've measured f_{pe} to be approximately 1.2MHz (indicating an electron density of 1.5× $10^4 cm^{-3}$), and calculated f_{ce} to be 1.26MHz from the IGRF magnetic field model.

$$\cos^2(\phi_r) = (\frac{1+R}{R})z - (1-z)\xi - z^2/R \tag{2.12}$$

Applying the ratio of our lower (upper) limit perpendicular wavelengths estimates to our directly measured parallel wavelength estimate, we obtain upper (lower) bounds on the observed VLF hiss wave-normal angle. These bounds, along with the theoretical resonance cone angle, are plotted as a function of frequency in the panel B of Figure 2.10. We note both the expression for ϕ_r and our interferometric observations refer to the phase-velocity resonance cone. For whistler waves propagating near the resonance cone the group velocity is perpendicular to the phase velocity forming a group velocity cone whose angle is the complement of the phase velocity cone [*Fisher and Gould*, 1971]. It is this group velocity cone that is observed in VLF saucers. From our phase velocity cone angle measurements we deduce the group velocity (power flow) of VLF

hiss waves to be between .5 and 2.0 degrees with respect to $\mathbf{B}_0$. There is some evidence of saucer structure between 375s and 450s in Figure 2.4, where the peak in the wave power above f_{LH} decreases in a roughly parabolic shape.

The predominant generation mechanism for VLF hiss has been identified as coherent beam amplification of whistlers by the auroral electron beam where these whistlers are seeded by incoherent Cherenkov radiation from the electron beam [*LaBelle and Treumann*, 2002]. The parallel wavelength is determined by the Cherenkov radiation condition,$k_{\|} = \omega/v_{\phi}$, where v_{ϕ} is the electron velocity. Panel A of Figure 2.11 shows the calculated resonant electron velocity as a function of frequency for our measured parallel wavelengths. These energies range from 10keV at 8kHz to 45keV at 20kHz. The highest energy electron spectrograph channel was ~ 5keV so we would have been unable to observe electrons with these energies. These energies are startlingly high for the aurora and can be explained a number of ways. Neither the VLF hiss nor the electrons are generated at the rocket's ~550km altitude. The resonance calculation ignores all refraction as the VLF hiss traversed the gradual ionospheric magnetic field and electron density gradients. As pointed out by *Ergun et al.* [1991] and *LaBelle and Treumann* [2002] the parallel index of refraction generally increases as a function altitude. This means that the parallel wave number is also an increasing function of altitude, and therefore the resonant electron energy decreases as a function of altitude. A full ray-tracing code with an accurate ionospheric model could be used to remotely sense the unstable electron distribution, but this is outside the scope of this paper.

A second explanation for the long observed wavelengths is that they could be due to scattering off of LHSS. One mechanism that allows VLF hiss to reach

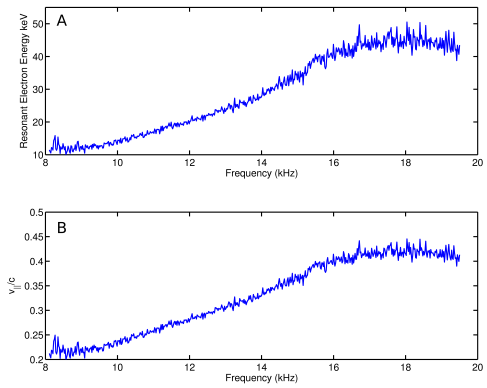

Figure 2.11: (A) The resonant electron energy. (B) Parallel phase velocity.

the ground is scattering by meter scale densities structures [**?**]. When VLF hiss scatters off of the density irregularities its wavevector can change from nearly perpendicular to nearly parallel, and this scattering process may also change the VLF hiss wavelength. The finite slope in inferred electron energies could mean either that there is a range of unstable electron energies, contrary to the assumptions made in *Ergun et al.* [1991], or that VLF hiss is being generated over a range of altitudes.

Panel B of Figure 2.11 shows the parallel phase velocity as a function of frequency normalized by the speed of light which is between 0.2c at 8kHz and 0.44c at near 20kHz. These correspond to parallel indices of refraction between 2.2 and 4.0, in close agreement of those predicted in *LaBelle and Treumann* [2002].

There are two key assumptions in our model of VLF hiss as it pertains to the cold plasma dispersion relation presented above. First, the conical wave vector distribution of electrostatic waves describes both the propagation direction of the waves and their polarization. Second, the random phase approximation that was used to simplify the expression for the cross-spectral product is justified by

both the isotropic perpendicular wavelength distribution of VLF hiss and by its generation via incoherent Cherenkov radiation. These two assumptions are verified experimentally in Figure 2.7, which shows near zero coherency where our model predicts it.

2.7 Conclusions

Using a multiple payload sounding rocket mission we've successfully measured the parallel wavelength of VLF hiss and bounded the perpendicular wavelength of VLF hiss. By calculating the interferometric response of two separated, arbitrarily oriented VLF wave antenna/recievers, we predicted nulls in the inter-payload coherency pattern. Observation of these nulls gave an upper bound estimate on the perpendicular wavelength of VLF hiss of $\sim$ 345m. Using a single payload interferometer, we confirmed previous perpendicular wavelength estimates of $\sim$ 60m. We also showed that the inter-payload phase spectrum was entirely a function of the inter-payload separation distance allowing for accurate estimation of the parallel wavelength of VLF hiss as a function of frequency of $\sim$ 6 – 8km. This constitutes one of very few parallel wavelength observations of space plasma waves. By combining our upper (lower) perpendicular wavelength estimates we computed lower (upper) estimates on observed wave normal angle which effectively bound the resonance cone angle predicted by cold plasma theory, verifying that VLF hiss falls on the whistler wave resonance cone.

CHAPTER 3

MULTI-PAYLOAD SOUNDING ROCKET OBSERVATIONS OF SMALL SCALE ALFVÉN WAVES AT THE POLAR CAP BOUNDARY

3.1 Abstract

We present observations from the multi-payload Cascades2 sounding rocket mission. For ~60km south of the polar cap entry the payload array encountered a region of intense, Alfvénic aurora. This aurora was characterized by large, fluctuating electric and magnetic fields, field aligned wave accelerated electrons, transversely accelerated ions, and Broad Band Extremely Low Frequency (BB-ELF) plasma wave emission. We performed inter-payload interferometry using a wavelet based local frequency-wavenumber decomposition that determined the electromagnetic fluctuations were moving 8km/s Westward across the payloads. We analyzed the DC electric field fluctuation spectra and found two breakpoints in the spectral slope. The first occurred between $k\lambda_e > 1$ and $k\rho_i < 1$, where λ_e is the electron inertial length, ρ_i is the larmor radius, and $\lambda_e > \rho_i$. The second breakpoint occurred at $k\rho_s = 1$ where ρ_s is the acoustic radius at electron temperature. From DC to the first breakpoint we observed a $k^{-1.77}$ power law, from the first breakpoint to the second we observed a k^{-5} power law, and beyond the second breakpoint we observed a k^{-2} power law. In the noisier magnetometer measurements we observed a $k^{-2.37}$ power law. We used orthogonal electric field observations to calculate the degree of polarization which revealed two distinct types of BB-ELF fluctuations; the first from DC to $k\rho_s < 1$ was wavelike with a degree of polarization above 0.7 and the second for $k\rho_s > 1$ was characterized as spatial structure, with a degree of polarization

below 0.7.

3.2 Introduction

Since inertial Alfvén waves were shown by *Goertz and Boswell* [1979] to carry a parallel electric field, $E_{\|}$, and thus accelerate auroral electrons, their propagation, interaction with the ionosphere and auroral acceleration region, and dispersion have been invoked to explain auroral structuring on all observed scales (see *Stasiewicz et al.* [2000b] for review). The dispersion relation for inertial Alfvén waves is given by Equation 3.1, where $\lambda_e = c/\omega_{pe}$ is the electron inertial length, $V_a = B/\sqrt{\mu_0 \rho}$ is the Alfén velocity, ρ is the plasma mass density, c is the speed of light and ω_{pe} is the plasma frequency.

$$\omega^2 = \frac{V_a^2 k_{\|}^2}{1 + k_{\perp}^2 \lambda_e^2} \tag{3.1}$$

At large scales, simulations and observation have shown that Alfvén waves launched in the magnetotail can be reflected off of the ionosphere creating ultra-low-frequency field line resonances [*Streltsov and Lotko*, 1995]. These field line resonances have been observed as 1-2mHz oscillations in ground magnetometers, and have been associated with auroral features having meridional scales of 10s of km. Multiple bounces of an Alfvén wave from a moving source magnetospheric source has been postulated as the origin of multiple arc systems (*Lysak* [1985],*Mallinckrodt and Carlson* [1978]).

Steep vertical gradients in Alfvén speed are known to exist at the top of the ionosphere and in the auroral acceleration region at near ~6000km altitude. These gradients have been shown to set up a resonant cavity termed the

ionospheric Alfvén resonator, whose fundamental frequencies are in the .1-1Hz range, and has been associated with 1-10km scale auroral arcs [*Chaston et al.*, 2002a].

Using a survey of high resolution auroral imagery, *Trondsen and Cogger* [1998] showed that the most probable thickness of an auroral arc element is ~ 200m. Using a database of FAST satellite passes and an MHD model *Chaston et al.* [2003] accurately predicted the width of auroral arcs driven by inertial Alfvén waves which matched the observed optical distributions. *Semeter and Blixt* [2006] related the smallest scale, ~100m, auroral arcs to inertial Alfvén wave dispersion. The size, shape, and motion of small scale auroral curls have been used to remotely sense the auroral acceleration region [*Hallinan*, 1981]. Due to the dipolar r^{-3} decrease in Earth's magnetic field strength, these studies relied on mapping factors to relate the observed auroral motion and size to acceleration region plasma parameters. The electric field mapping was to proportional to $\sqrt{B}$, while the velocity and scale size mapping factors were proportional to $1/\sqrt{B}$.

Its been shown that inertial Alfvén waves are responsible for a significant portion of observed ion and electron acceleration in the auroral region [*Chaston et al.*, 2007]. Electron acceleration in inertial Alfén waves has been extensively studied. *Kletzing* [1994] showed that Alfvén waves could resonantly accelerate electrons up to twice the Alfén velocity. This model was latter shown to accurately describe the observed electron energy time dispersion [*Kletzing and Hu*, 2001]. Electron acceleration via Alfvén wave breaking was shown by [*Hui and Seyler*, 1992] to accelerate electrons up to twice the Alfén velocity under magnetospheric (~ 1 Re) conditions. Similarly, *Clark and Seyler* [1999] showed that electrons can be trapped in the Alfvén steepening and breaking process, leading

to the formation of electron beams. *Watt et al.* [2005] showed that Alfvén wave steepening can cause non-resonant electron acceleration.

Using a survey of FAST observations *Chaston et al.* [2007] attributed 15-36% of ion outflow to inertial Alfvén wave energy deposition. *Chaston et al.* [2002b] have shown that inertial Alfvén waves can directly accelerate ions to the observed outflow energies through a combination of coherent gyroresonant wave-particle interactions and incoherent stochastic acceleration. Alfvénic structures have been frequently observed to be collocated with Broadband Extremely Low Frequency (BB-ELF) plasma wave emissions [*Knudsen et al.*, 1998b]. It has been shown by *André et al.* [1998] that field aligned currents in the auroral zone are generally too low to directly destabilize the current driven ion-acoustic and ion-cyclotron instabilities predicted by *Kindel and Kennel* [1971]. Consequently, generation of BB-ELF by dispersive Alfvén waves has received significant experimental and theoretical attention. *Wahlund et al.* [1998] showed examples of intense BB-ELF emission and high ion temperatures within Alfvénic structures, and termed the BB-ELF emissions slow ion acoustic (SIA) waves. In nonlinear simulations, *Seyler et al.* [1998] showed that these emissions could be explained by an ion-Boltzman density response to Alfvén wave steepening and breaking. *Stasiewicz et al.* [2000a] and *Klatt et al.* [2005] examined the observed $\delta E/\delta B$ ratios from satellite and sounding rocket measurements, respectively, to show that the BB-ELF plasma waves are Doppler shifted, small-scale Alfvénic structures.

The tearing mode instability, a three dimensional instability driven by parallel currents and due to dispersion at the electron inertial scale, was first introduced to explain the dynamics and morphology of discrete auroral arcs by *Seyler* [1988] and extended to a realistic ionosphere by *Seyler* [1990]. Later, *Seyler and*

Wu [2001] presented a closely related instability, termed the current-convective instability which occurs near points in an inertial Alfvén wave where $\mathbf{k} \cdot \mathbf{B}_0 = 0$ to explain BB-ELF. Taken as a whole, this class of current shear related instabilities can address the formation of an auroral arc, its evolution into auroral curls, and the generation of BB-ELF.

3.3 Experiment Setup

The Cascades2 sounding rocket was launched at 11:04:00 UT on March 20th, 2009 from the Poker Flat Research Range outside of Fairbanks, Ak. into a pre-midnight Poleward Boundary Intensification [*Mella et al.*]. The sounding rocket was composed of five instrumented sub-payloads: one main payload, two Cornell wireboom electric field sub-payloads (FWD and AFT), and two particle free fliers (PFF1 and PFF2). The electric field subpayloads were ejected at high velocity, 15m/s, along their spin axes. An inertial attitude control system aligned the spin axis at sub-payload ejection to minimize the angle between the sub-payloads' separation vector and the magnetic field at apogee. The two PFFs were ejected in the plane perpendicular to $\mathbf{B}_0$ such that the vectors between each PFF and the main payload formed right angle. During powered flight the restraining cable on PFF2 was inadvertently severed, which gave it a higher ejection velocity than PFF1 and destroyed its particle detector.

Each payload was equipped with a GPS receiver that provided accurate absolute, and relative position information, and ensured synchronous timing. The payloads' positions and velocities were transformed into a local Vertical-East-North coordinate system where the x-axis is aligned opposite to the local mag-

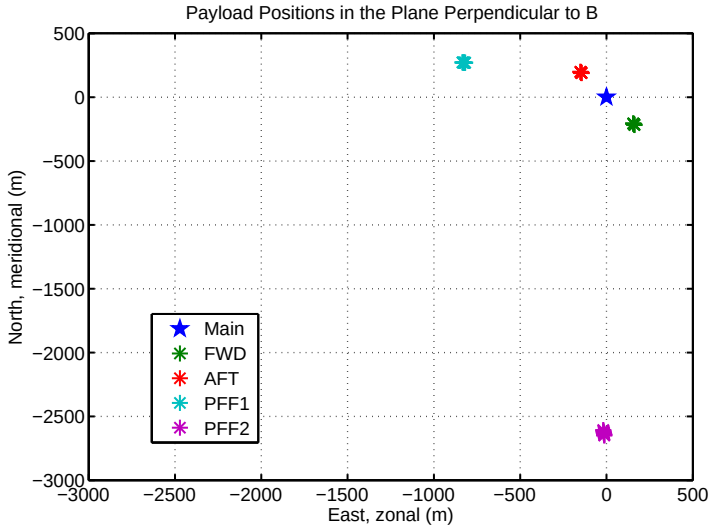

Figure 3.1: Relative positions of the five Cascades2 payloads in the plane perpendicular to $\mathbf{B}_0$

netic field, the z-axis points meridionally towards the magnetic pole, and y-axis points zonally completing the right-handed triad. The payloads' relative positions in the plane perpendicular to $\mathbf{B}_0$ are shown in Figure 3.1 with the Main payload placed at the origin. The electric field sub-payloads were separated ~ 6.5km along $\mathbf{B}_0$, and ~ 500m in the plane perpendicular to $\mathbf{B}_0$. The main payload was situated between the two subpayloads. Data presented herein come from a 8 second period of the flight on the downleg when the main payload's altitude was ~ 445km. The payloads' velocity in the plane perpendicular to $\mathbf{B}_0$ was ~1480m/s pointing 52.2 degrees West of North.

Data presented herein were taken by the two Cornell electric field sub-payloads and the main payload. The electric field measurements on the sub-payloads were made by a pair of crossed 12.12m dipoles formed by taking the potential difference between 4.45cm diameter spheres at the ends of coaxial wire-booms. Each sphere pair was connected to three different plasma wave receivers. The

DC coupled channels recorded from DC to 1kHz, and were de-spun into the Vertical East North coordinate system using a modified version of the attitude determination filter/smoother described in *Humphreys et al.* [2005]. The VLF channels recorded between 20Hz and 40kHz (with a Nyquist frequency of 20kHz). One sphere pair on each payload was equipped with an HF snapshot receiver, which recorded 4096 samples at 4.8MHz once every 10 milliseconds.

The main payload was equipped with three particle detectors, two that probed the electrons and one that probed the ions. The HEEPSe electron detector was swept over 64 logarithmically spaced energy steps between .1eV and 5keV once every 64ms and sampled the full pitch angle distribution. The high time resolution Bagel detector was swept between 1eV and 1keV once every 8ms and had a narrow, three degree half width, aperture aligned to the main payload spin axis (see [*Mella et al.*] for details). The ion detector was swept between .1eV and 800eV once every 64ms seconds and sampled the full pitch angle distribution. There was no mass discrimination on the ion detector.

Magnetometer data were taken from a deck mounted science magnetometer on the main payload. These data were despun using the attitude knowledge from the inertial ACS. Upon removal of gyro drift effects using the algorithm in *Psiaki* [2002], large, ~500nT, spin related variations were still apparent. An FFT analysis revealed spurious power at the spin frequency and many higher order harmonics. A series of 20 digital narrowband filters were used to remove these payload motion and instrument interference related effects. Due to this extensive post processing, we urge caution in interpreting the magnetometer data.

3.4 Observations

To contextualize the rocket observations we begin by summarizing the observations of the Kaktovic narrow field auroral imager. A thorough analysis of these observations and their connection to the *in-situ* electron measurements is the subject of a companion paper[*Lynch et al.*, 2011]. This narrow field imager was attached to a swivel mount which allowed it to track the passage of the rocket. During the ~40s (~64km) preceding entry into the polar cap the experiment array encountered a region of intense, Alfvénic aurora. This occurred at a latitude of 72.5 degrees North, 2.5 degrees North of Kaktovic (70.133° N, 143.6° W), which gave the imager an oblique view of the aurora. The optical aurora was composed of tall, rapidly moving, long lived "rays". Each ray had an approximately ~2km width in the imager plane which was nominally aligned perpendicular to the magnetic meridian. The individual ray velocity was +/- 8-10 km/s in this plane. The lifetime of each ray was on the order of 5-10s, but varied substantially. Due to the oblique look angle of the camera, meridional information about ray location and velocity is unobservable. This oblique look angle blurred the sub-structure within each ray perpendicular to $\mathbf{B}_0$.

Figure 3.2a presents the DC electric field measurements from FWD and AFT sub-payloads (solid and dashed lines, respectively), in the magnetic East and North (blue and red, respectively) direction. Figure 3.2b shows the magnetic field from the main payload. Figure 3.2c shows the electron energy integrated over all pitch angles. Figure 3.2d shows the ion energy integrated over all pitch angles. Figure3.2e shows the VLF wave electric field between 20Hz and 20kHz from the AFT payload. The payload array entered a brief region of Alfvénic activity 584s into the flight that persisted for 6s. The activity resumed at 599s

and continued for ~ 30s until the payloads entered the polar cap. To focus on the medium and small scale physics, we present observations from the 8s period from 598s to 606s, which contained the largest DC electric and magnetic field fluctuations, and most intense particle fluxes.

The largest peak-to-peak electric field variations were approximately 330mV/m which occurred over .4s at 602.5s. Coincident with these large electric field variations were large magnetic field variations, on the order of ~150 nT. The $\delta E/\delta B$ ratio was $\sim 1.5 * 10^6$m/s, similar to the mass density derived Alfvén velocity, Va = $2.0 * 10^6$m/s. There were three sources of density information: 1) the lower hybrid resonance, identified by the cutoff in power near 5kHz in VLF wave data 2) observations of langmuir wave emissions captured by HF wave snapshot receivers on the sub-payload and 3) moment analysis of the ion pitch angle distribution functions. Each of these methods indicated plasma densities around $1.5 * 10^4$ cm^{-3}. Detailed comparison of the lower hybrid frequency and plasma frequency by *Lundberg et al.* indicated 2.5-3.0% H^+ concentration in an otherwise O^+ plasma.

Each sub-payload was equipped with an electron retarding potential analyzer that accurately measured the electron temperature, which increased from .2eV to .5eV during this region (see *Mella et al.* for details). Detailed analysis of the ion data revealed a few distinct populations. The background ionosphere was cool and had a temperature of ~ 1.0eV. Due to the wide energy of the detector the it was saturated by the thermal ion population which accounts for the red bar at 1-3eV in 3.2d. In places the plasma drift velocity exceeded the rocket velocity which made the effective ram-vector highly variable and obscured detailed pitch-angle information perpendicular to $\mathbf{B}_0$. We observed a higher en-

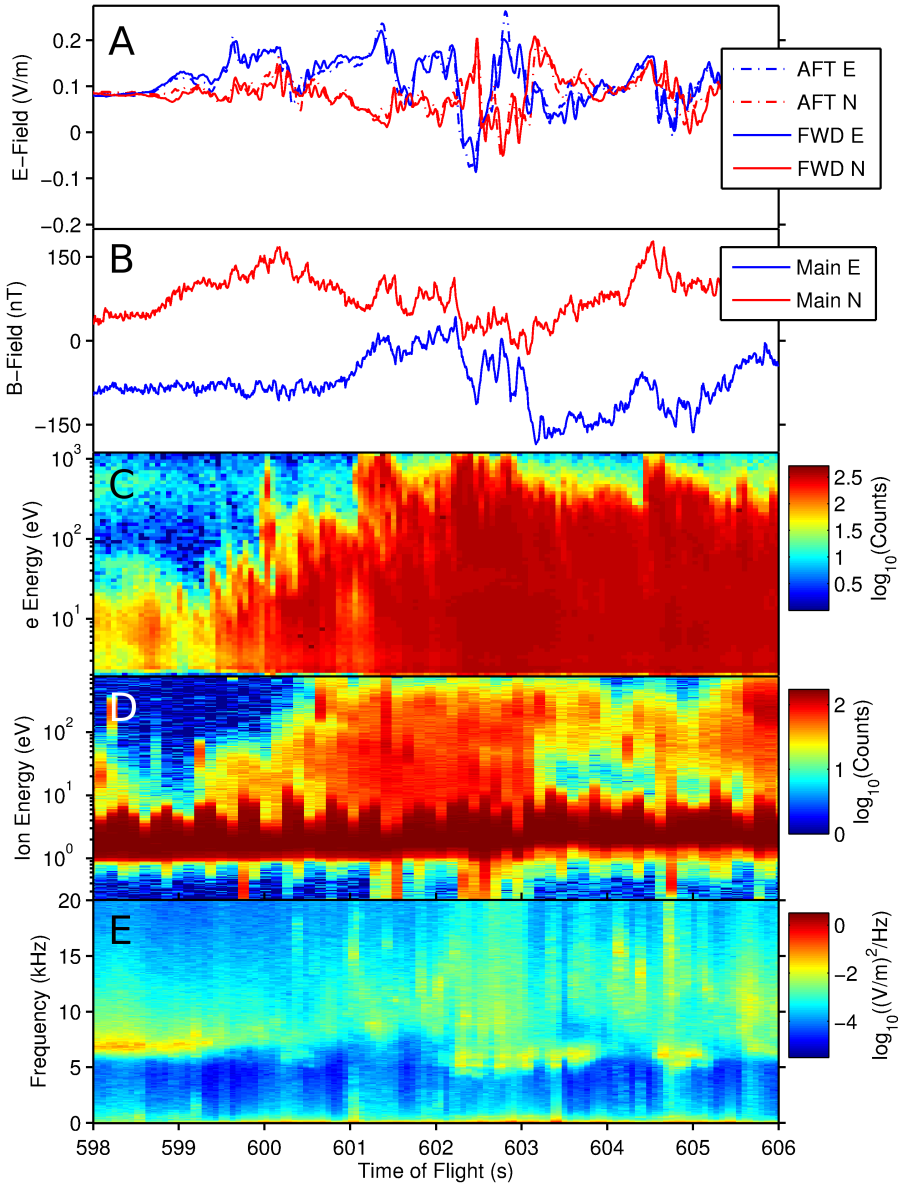

Figure 3.2: Overviews of the observed fields and particles. (A) The observed DC electric field in plane perpendicular to $\mathbf{B}_0$ from both subpayloads; (B) the magnetic deflection from the main payload; (C) electrons integrated over all pitch angles from the main payload; (D) ions integrated over all pitch angles from the main payload; (E) VLF plasma waves from the AFT payload.

ergy, 100eV, ion population that was primarily coming down the field line. Detailed analysis of these measurements can be found in [*Lundberg et al.*].

The plasma wave observations were highly structured near the lower hybrid resonance, f_{lh}, with values ranging from 5kHz to 7kHz. Below f_{lh}, there existed BB-ELF wave emissions from 20Hz-1kHz, a narrowband wave emission at the H^+, O^+ resonant frequency, and a few broadband, impulsive features, similar to lower hybrid solitary structures (LHSS).

The DC electric and magnetic fields and electrons all exhibited apparent modulation on two time scales, .5-1Hz and ~8Hz. In the electron data, the lower frequency oscillation was observed as a modulation of the peak electron energy, while individual electron bursts were modulated at ~8Hz. We isolated the higher frequency modulation in the electric field signal by high pass filtering it above 4Hz using a 4-pole digital butterworth filter. Figure 3.3a shows the electron energy from the high time resolution electron detector between 1eV and 1keV. Figure 3.3b shows the filtered Eastward electric field from the FWD and AFT payloads and Figure 3.3c shows the filtered Northward electric field. There existed a strong correlation between these electric field signals and the observed electrons. The filtered electric field signals exhibited a "spiky" waveform which is indicative of wave steepening. Visual inspection of the filtered waveforms showed strong similarity between the payloads indicating the some of the 8Hz oscillation in the spacecraft frame is due to temporal variations in the plasma frame. (A detailed cross-spectral analysis will be presented later in this paper).

Lynch et al. [2011] and *Mella et al.* calculated source altitudes for these suprathermal electron bursts. They identified 27 electron bursts with an average source altitude of 661km, a minimum altitude of 529km and maximum altitude

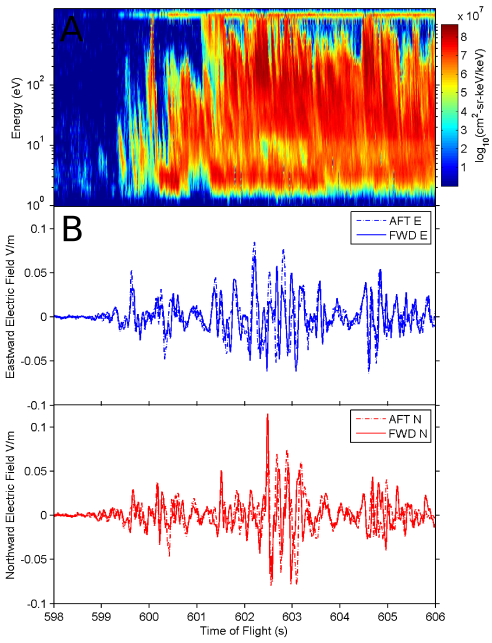

Figure 3.3: The high time resolution electron observation (A) and high pass filtered electric fields (B and C).

of 1033km, referenced to the surface of earth. The temperature of these beams were all less than one eV. Comparison of the observations by the two electron detectors revealed that most, but not all, of these electron bursts fell within the 1keV range of the Bagel detector.

Figure 3.4a shows the local frequency-wave number decomposition calculated over the entire 598-606s period comparing the Eastward electric fields on the FWD and AFT payload. The local frequency wavenumber decomposition, which was first introduced by *Dudok de Wit et al.* [1995b], utilizes the high frequency-time resolution of the wavelet transform to calculate the interferometric phase between two sensors. This phase, ϕ, can then be related to the projection of the wavevector along the line of sight between the two payloads, $k_d = \phi/d$, where d is the interpayload separation distance. A histogram of the

phases is formed and multiplied by the wavelet power at each phase. Following *Schuck et al.* [1998] we used the morlet mother wavelet with frequency, ω_0 = 5.36, and bandwidth of two. In these calculations we assumed that all variation in the observed electric field is due to the sub-payloads' ~ 500m perpendicular separation, which is valid as a structure moving at the Alfvén velocity would have traversed the subpayloads' 6.5km separation parallel to $\mathbf{B}_0$ in ~ 3ms, which would cause a phase shift of less than 1 degree at these frequencies. The diagonal white lines correspond to the frequency that would have been measured do to the Doppler shift, $2\pi f_{sc} = k v_{sc}$, of the wavenumber on the x-axis. Below where these lines intersect the y-axes, at f_{sc}= 3.5Hz, is where we were able to unambiguously determine phase velocity, as a purely spatial wave in the plasma frame Doppler shifted to this frequency would have caused a +/- π interferometric phase shift. Figure 3.4b shows the interferometric coherency over the entire 8s time period and over selected sub-intervals.

The salient features of Figure 3.4 are the organized phases (wavelengths) below 3.5Hz and the oppositely directed (positive and negative) phases at +/- k_d ~.002 above 3.5Hz. The black line corresponds to the phase shift due to a wave that had a 8km/s phase velocity moving Westward across the payloads. This was calculated assuming all motion was meridional and is only valid for structures larger than interpayload separation distance. Above 3.5Hz, the phase had both positive and negative values. As detailed in Figures 3.5 and 3.6, these phase reversals were structured. First from 599.5s to 600.6s, the inter-payload phase above 3.5Hz was positive (3.5b), and then, from 600.7s to 601.4s the inter-payload phase was negative, as shown (3.5c). This positive-to-negative phase pattern was repeated over the next 2s, the period between 601.8 to 602.6 was positive (3.6b), and the period between 603.7s and 603.4s was negative (3.5c).

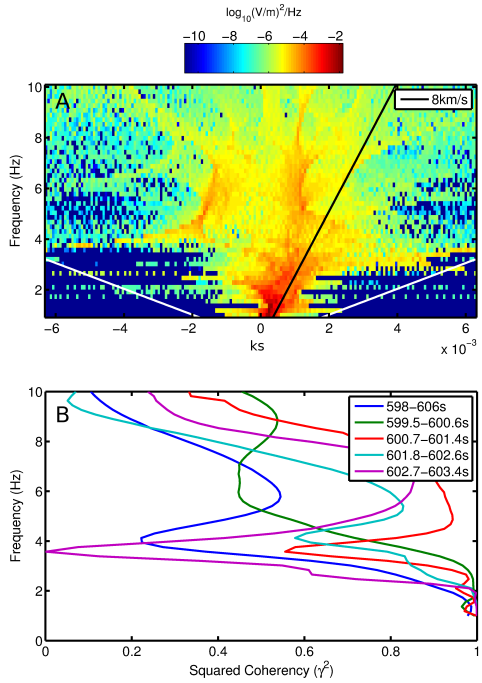

Figure 3.4: (A) The local frequency wavenumber decomposition for the entire 598-606s time period. (B) The interferometric coherency over 598-606s time period and selected sub-intervals.

From 603.4s to 606s the phase was always positive.

The inter-payload coherency can be used as a gauge of the reliability of these wavelength estimates [*Labelle and Kintner*, 1989]. Over the the entire 8s region the inter-payload coherency below 3.5Hz was always quite large, above 0.7. Calculating the inter-payload coherency above 3.5Hz over the entire 8s led to a lower value of .5. However, when we sectioned our coherency calculation to correspond to the regions of positive and negative phase shift, we obtained large coherency values above 3.5Hz. At 3.5Hz, the coherency was always low. There are two interpretations of these data. The first is that this phase reversal was due to a true changing in the orientation of the phase velocity direction with respect to the inter-payload separation vector. The second, and more likely, explanation

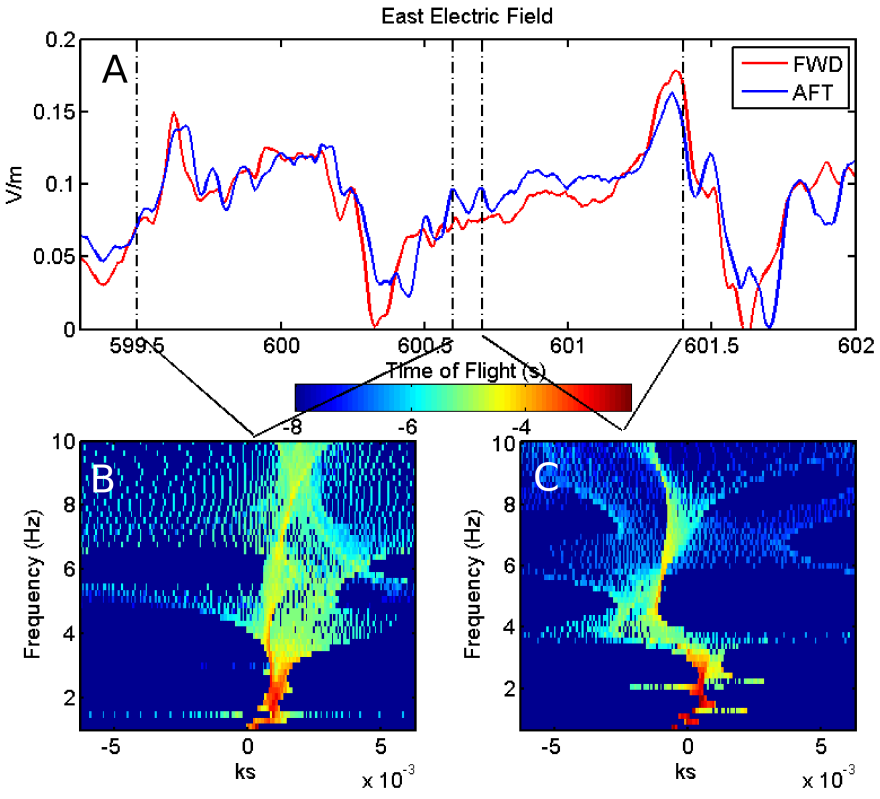

Figure 3.5: (A) The Eastward electric field for both subpayload between 599. and 602s (top panel). (B)The local frequency-wavenumber decomposition from 599.6s to 600.6s and (C) 600.7s to 601.4s.

is that below 3.5 Hz we can unambiguously measuring the perpendicular phase velocity of auroral structures past the payloads, but above 3.5Hz the frequency measured was partly due to the wave frequency and partly due to doppler shift of waves with wavelengths shorter than the interferometer baseline. Occasionally, authors have been able to observe phase wrap around and interferometric nulls which allow them to measure wavelengths shorter than the sensor separation distance, but no nulls were clear in our data (*Chaston et al.* [2005b],*Kintner et al.* [1987]). The correspondence of the coherency null at 3.5Hz, where the measured spacecraft frame frequency is equal to the doppler shift due to interferometer length spatial structures, leads us to believe the second interpretation

is more likely. Traditional interferometry has assumed that the measured frequency is due to either doppler shift, or wave frequency [*Labelle and Kintner*, 1989]. The spacecraft frame frequency is given by $f_{sc} = f_{wave} - k_{wave} * v_s/(2\pi)$. For plasma waves whose $\omega - \mathbf{k}$ dispersion relation is nonlinear, e.g. $\omega \propto k^{\alpha}$ where $\alpha \neq 1$, the possibility exists for multiple waves to have the same spacecraft frame frequency. (Note the use of the term nonlinear is only used to define the mathematical relationship between ω and $\mathbf{k}$ and does not refer to wave dispersion due to physical nonlinearities). In this case the interferometric phase would be a function of wavelength, frequency and wave amplitude, complicating its interpretation.

Figure 3.7a shows the ratio of the electric to magnetic field fluctuations, $|\delta E/\delta B|$, normalized to the local Alfvén speed versus perpendicular wavenumber, normalized to the local electron skin depth (black stars). The reported perpendicular wavenumber was determined using the assumption that all measured variations are due to Doppler shift. The blue line corresponds to the Alfvén wave dispersion relation given in Equation 3.2, with the parameters given in Table 3.1. Figures 3.7b and 3.7c compare orthogonal electric and magnetic fields. Figure 3.7b compares the Eastward electric field with the negative of the Northward magnetic field, and Figure 3.7c compares the Northward electric field with the Eastward magnetic field. For the lower frequency oscillations, the electric and magnetic fields were apparently 180 degrees out of phase, indicating these fluctuations were traveling waves [*Knudsen et al.*, 1992].

Figure 3.7d shows the density derived from observations of Langmuir wave emissions on the HF wave snapshot receivers from both payloads. The temporal resolution of these measurements was limited to one sample every 9.87ms.

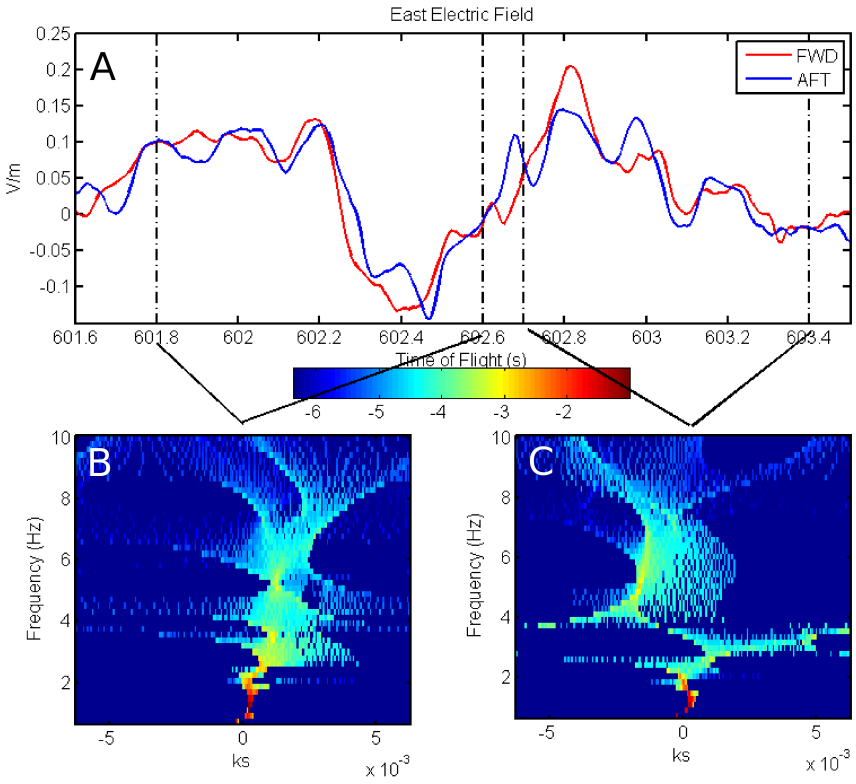

Figure 3.6: (A) The Eastward electric field for both subpayload. (B) The local frequency-wavenumber decomposition from 601.8s and 602.6s and (C) 603.7s and 603.4s.

These data were picked by finding the frequency bin of a 4096 point FFT with the highest power so their resolution is coarse. Between the two payloads, the FWD payload almost always measures lower density. The average difference between FWD and AFT over this 8s period is $2*10^3 cm^{-3}$. By assuming all vertical variation is due to an exponential scale height dependence, $n(r) = n_0 \exp(-r/H)$, where r is altitude above the surface of the earth, n_0 is the electron density at some reference height, and H is the ionospheric scale height, we used the ratio of density measurements and the known payload positions to estimate the ionospheric scale height to be 300km.

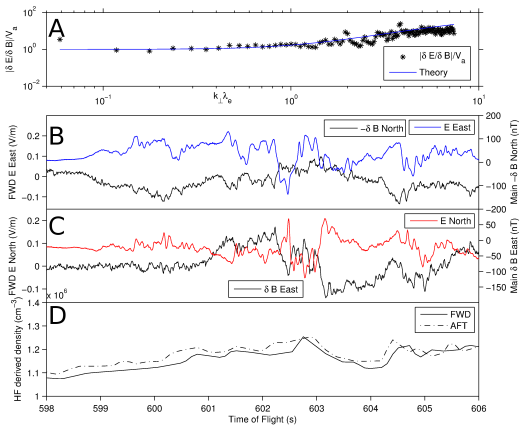

Figure 3.7: (A) The measured ratio of electric to magnetic field normalized to λ_e. Comparison of orthogonal electric and magnetic fields; (B) the Eastward electric field and negative of the Northward magnetic field and (C) the Northward electric field and Eastward magnetic field. (D) The density estimates from the two sub-payloads.

The blue dots in Figure 3.8a shows the power spectral density for the Eastward electric field from the AFT payload. The lower x-axis shows the measured spacecraft frame frequency, and the upper x-axis shows the corresponding perpendicular wavenumber. The green dots are the VLF wave power from the AFT payload. The roll off below f_{sc} =20Hz in the VLF measurement was due to the high pass filter on this channel. There were two distinct break points in the power spectral density, the first at $f_{sc} \sim$ 8Hz, and the second at $f_{sc} \sim$ 40Hz. We performed linear fits to the three regions defined by these breakpoints. From 1Hz to 8Hz, 8Hz to 40Hz, and from 40Hz to $\sim$ 130Hz the spectral slopes were -1.78+/-.028, -5.01+/-.04, and -1.99+/-.006 , respectively. We chose 130Hz as the upper limit for the third fit as it is the frequency where finite antenna length effects become important. We calculated similar figures in each direction and on each payload, all of which showed similar trends. The second breakpoint was consistent between the two electric field receivers which demonstrated the

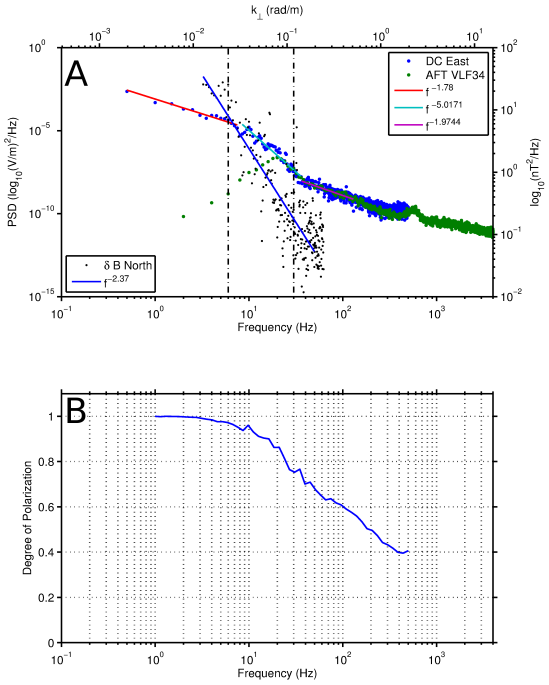

Figure 3.8: Power spectral density for the DC and VLF electric field channels (top panel) and percent polarization (bottom panel).

validity of the higher frequency components of the DC coupled receiver. The black dots are the power spectral density of the Eastward electric field and corresponds to the values on the right y-axis. The spectral slope was calculated from 2Hz to 50Hz and was -2.37+/-.1. Note the right and left y-axes of Figure 3.8a have different spans. Figure 3.8b shows the degree of polarization of the electric field signal in the plane perpendicular to $\mathbf{B}_0$ [*Samson and Olson*, 1980]. The degree of polarization was defined by *Samson and Olson* [1980] as the ratio of polarized power to total power with the polarized power being determined by how much of the signal preserves a constant phase relationship, and has been used to distinguish between plane waves and spatial structures (*Chaston et al.* [2005a], *Sundkvist et al.* [2005]).

Quantity	Value	Expression
$n_e \approx n_i$	$1.2 - 1.5 * 10^4 cm^{-3}$	-
T_e	.2-.5eV	-
T_i	.5-1.0eV	-
v_{the}	$.42 * 10^6$m/s	$\sqrt{2k_bT_e/m_e}$
c_s	775-1734 m/s	$\sqrt{k_bT_e/m_i}$
V_A	$1 - 2 * 10^6$m/s	$B/\sqrt{\mu_0\rho}$
λ_e	40-50m	$\sqrt{m_e/n_0\mu_0e^2} = c/\omega_{ce}$
λ_i	7500-8500m	$\sqrt{m_i/n_0\mu_0e^2} = c/\omega_{ci}$
ρ_s	2.6m	c_s/ω_{ci}
ρ_i	25m	$m_iv_\perp/qB$
ω_{ci}	$2\pi * 44$Hz	qB/m_i
β	$2.5 * 10^{-5}$	$nk_bT/(B^2/2\mu_0)$

Table 3.1: Relevant observed and derived plasma parameters for the Cascades2 sounding rocket mission.

3.5 Discussion

The Alfvénic nature of this event is confirmed in the top panel of Figure 3.7 which favorably compares the observed ratio of the electric and magnetic field fluctuations to that predicted by the Alfén wave dispersion relation. This dispersion relation, which includes thermal effects, is given by Equation 3.2

$$\left|\frac{\delta E}{\delta B}\right| = V_a \sqrt{\frac{(1 + k_\perp^2\lambda_e^2)(1 + k_\perp^2\rho_i^2)}{(1 + k_\perp^2\rho_s^2)}} \tag{3.2}$$

where the values and expressions forρ_s, the acoustic length, and ρ_i, the larmor radius are given in Table 3.1. *Klatt et al.* [2005] and *Stasiewicz et al.* [2000a] calculated the phase between δE and δB and determined that for $k\lambda_e < 1$, this phase is near 180 degrees which indicated propagating waves, and for $k\lambda_e > 1$ the this phase tended towards 90 degrees which indicated spatial structures. For Cascades2, the large scale electric and magnetic fields, shown in second and third panels of Figure 3.7, were apparently 180 degrees out of phase. However, since the separation between the reliable magnetometer on the main payload and the

electric field sensors on the subpayloads was near $1\lambda_e$ analysis of this cross spectral phase was impractical.

Since the electrons responsible for the auroral light are tied to the magnetic field, we expect the auroral motion to accurately reflect the plasma dynamics where the electrons are accelerated. The observed 8km/s speed of the tall auroral rays would predict electric fields of +/-400mV/m if their motion was determined by the local $E \times B$ drift velocity, which is a factor of two larger than what we observed. Neither the $\sqrt{B_0}$ mapping factor of *Hallinan* [1981] nor shorting of electric fields by ionospheric conductivity [*Spreiter and Briggs*, 1961], can account for the totality of this difference as they would attenuate the electric field by 10% and at most 20% between the electron source altitude and the rocket. This suggests that the ray velocity was controlled by a phase velocity rather than the plasma drift velocity. Additional support for this comes from the inter-payload interferometry, which shows that the low frequency, 1-3.5Hz oscillations, were moving 8 km/s Westward. Due to the complex shape of the the vector-potential in Alfvénic aurora (see *Seyler* [1990] and *Chaston et al.* [2010]), the source region velocity may not have been observable in the electric field at the rocket altitude, making these results suggestive.

Inspection of the waveforms of Figures 3.5a and 3.6a reveal a complex relationship between which payload "saw" which disturbance first. For instance, between 599.5 and 600.6s, the DC electric field on the FWD payload leads AFT's. This relationship was reversed between 600.7 and 601.3s (Figure 3.5a). The apparent delay time between the payloads was always significantly smaller than the .3s traversal time over their perpendicular separation. As shown above, the delay between the 1. and 3.5Hz structures was plausibly due to the 8km/s

Westward ray motion. One interpretation of the reversal in inter-payload phase above 3.5Hz in Figures 3.5 and 3.6, which was a frequency space manifestation of changing delay times, was that the motion of the small structures that constitute each ray were moving in opposite directions with respect to the inter-payload separation vector. In places the amplitude and shape of the steepened structures on each payload are similar, indicating we observed time variations of structures larger than the inter-payload separation vector. Elsewhere, the steepened structures were dissimilar in amplitude and shape, indicative of scale sizes on the order of, or smaller than, the inter-payload separation distance. There are at least three plausible explanations for this oppositely directed phase velocity: 1) it could be a manifestation of the Alfvén wave resonance cone [*Semeter and Blixt*, 2006] which produces perpendicular phase velocities pointing radially inward towards its apex 2) it could be due to the rotation and non-linear evolution of the auroral forms [*Chaston et al.*, 2010] or 3) it could simply be an instrument artifact.

It has been show that Alfvén waves can resonantly accelerate electrons to up to twice the Alfvén velocity when the electron thermal velocity is close to the Alfvén velocity, $v_{the} \approx V_a$. In the auroral ionosphere, this condition is fulfilled in two regions. The first is the typical auroral acceleration region at 4000-6000km [*Kletzing and Hu*, 2001]. The second is topside ionosphere, which is usually considered for its ability to reflect Alfvén waves (*Seyler* [1990], *Knudsen et al.* [1992]), and absorb electrons [*Lysak*, 1991]. Simulations have shown that Alfvén wave steepening occurs when the Alfvén wave amplitude exceeds a certain threshold [*Seyler et al.*, 1995]. If the Alfvén wave carries sufficient parallel electric field, and there are sufficient resonant electrons, Alfvén wave breaking can occur [*Seyler and Liu*, 2007]. The wave breaking process can trap electrons which can cause

the electric field to develop bipolar signatures *Clark and Seyler* [1999]. Using an IGRF magnetic field model and our observed 300km scale height, we estimate that the V_a was $\sim 1 * 10^7$ m/s at our estimated electron source altitude. This is within a factor of two of our peak ~ 1keV ($1.9*10^7$m/s) electron energy. Between 602 and 603s in Figure 3.3 there is evidence that these bipolar structures existed. A purely spatial interpretation of the duration of these structures, about .15s, corresponds to a ~250m width at our 1470/s spacecraft velocity, which is approximately one electron inertial length ($2\pi\lambda_e$). This .15s duration corresponds to 6.6Hz, 2.6 Hz above the applied 4Hz butterworth filter, indicating they are real structures and not filter artifacts.

The first break point in the power spectral density, indicated by the left vertical, black, dashed-dotted line in Figure 3.8a, occurred at a spacecraft frame frequency of 8Hz, or a Doppler shifted wavenumber of .03 rad/m. This wavenumber falls between the $k\lambda_e$=1 and $k\rho_i$ =1, and the $k^{-1.79}$ power law leading up to it is indicative of large scale, MHD turbulence. A similar spectral break point and slope was identified by *Earle and Kelley* [1993] for sounding rocket data. Using a database of many satellite passes through the auroral acceleration region *Chaston et al.* [2008] found a similar $k^{-1.77}$ law for $k\lambda_e < .1$ in magnetic field power spectra. *Chaston et al.* [2008] identified a second break point at $k\rho_i = 1$ with a scaling law of $k^{-2.35}$ between $k\lambda_e > .1$ and $k\rho_i = 1$. This compares favorably to our magnetic field spectra. A discrepancy between our observations and those presented in *Chaston et al.* [2008], is that their steepest spectral slopes of $k^{-3.5}$ occurred beyond their second breakpoint, while our observed spectral slope became shallower at the second breakpoint. This may be due to comparing electric field spectra to magnetic field spectra. At the altitude of our observations the fluctuating magnetic fields contain ~ 10^4 more energy than the electric fields. A

similar flattening of the spectral slope beyond a second breakpoint was investigated by *Voitenko and De Keyser* [2011] for kinetic Alfvén waves and showed that the steep slope was due to weak wave dispersion, and the shallow slope was due to strong wave dispersion. Relating power spectral density measured on a moving platform to physical power density introduces ambiguities due to the relative orientation of the sensor and its velocity with respect to the irregularities and due irregularities' dispersion [*Fredricks and Coroniti*, 1976]. The apparent spectral breakpoints must therefore be interpreted with caution, as the first occurred at ~ 8Hz where we expect significant temporal variations due to the Alfvén waves, and the second occurred the O^+ cyclotron frequency.

The second break point in the electric field power spectral density occurred at a spacecraft frame frequency of 40Hz near the O^+ cyclotron frequency of 44Hz, or a Doppler shifted wavenumber of .15 rad/m, near the inverse ion sound length $k\rho_s = 1$. The steep, k^{-5}, power law indicates a rapid cascade of energy to shorter wavelengths (higher frequencies), which may be responsible for the perpendicular ion heating, and is similar to that observed in transient initial phase observed in simulations *Seyler* [1990]. Interestingly, *Voitenko* [1998] predicted a k^{-5} dependence for the forward enstrophy cascade in kinetic Alfvén waves. To investigate possible wave modes, we roughly estimate field aligned current, $J = 1/(\mu_0 v_{sc})\delta B/\delta t$, to our largest recorded magnetometer deflection. This deflection is ~ 150nT was recorded over .25s, 602s into the flight, and corresponded to field aligned current density of ~ $300\mu A/m^2$. This current density was sufficient to destabilize current driven ion cyclotron waves, but was insufficient to destabilize ion-acoustic waves *Kindel and Kennel* [1971]. *Seyler and Wahlund* [1996] identified $k\rho_s$ =1 as the breakpoint between ion-acoustic and ion-cyclotron waves with $k\rho_s < 1$ being ion-cyclotron, and $k\rho_s > 1$ being ion-

acoustic. They also introduced the terminology fast and slow to distinguish waves whose phase velocity is faster and slower than the acoustic speed, c_s.

Further information about the waves was given by the degree of polarization in the second panel of Figure 3.8. A degree of polarization above 0.7 means that the waves preserved a phase relationship between different components [*Chaston et al.*, 2005a], and a low degree of polarization, below ~0.7, would indicate structure [*Sundkvist et al.*, 2005]. For the large scale Alfén waves that accelerate the electrons, the degree of polarization was near unity. In the region where the spectral slope was steepest, the degree of polarization decreases to 0.7. The second breakpoint in the power spectral density coincides with the degree of polarization dropping below 0.7 indicating the fluctuations were no longer well described as plane waves. Simulations show that BB-ELF waves generated by Alfvén wave breaking generally appear to be a mixture of ion-cyclotron and ion-acoustic modes (*Seyler and Liu* [2007] and *Liu et al.* [2006]). These simulation studies calculated the ratio of electric field fluctuations to density fluctuations and showed that they lie on the curve given by Equation 3.3

$$\left|\frac{\delta E}{\delta n}\right| = \frac{1 + k^2\rho_i^2}{k\lambda_i} \tag{3.3}$$

where λ_i is the ion-inertial length. This relationship indicates that the density response is ion-Boltzman for scales shorter than ρ_i. *Liu et al.* [2006] simulated the evolution of a three dimensional Alfvénic structure and observed the emergence of vortices at the larmor radius scale which they attributed to the nonlinear evolution of current-shear driven instabilities.

The combined waveform, spectral and polarization analysis may indicate of the following situation; a large amplitude Aflvén wave propagated along the magnetic field and encountered the topside auroral ionosphere which had suf-

ficient thermal electrons to cause wave steepening. During this steeping process ion-cyclotron waves were emitted which were rapidly dissipated transferring energy from the Alfvén waves to the ions. At scales where $k\rho_s > 1$, the waves broke or evolved into structures that are no longer well described as plane waves.

3.6 Conclusions

This paper has four main observations that paint a compelling, nearly complete, picture of Alfvénic aurora.

1. In this event the top of the ionosphere the dominant source for auroral electrons.

2. Using multiple payload interferometer we show the motion of tall auroral rays may have been controlled by a perpendicular phase velocity and not the plasma drift velocity.

3. There existed steepened structures at the electron inertial scale that had significant temporal components and are causatively related to electron acceleration.

4. In the ion-Boltzman regime there existed two types BB-ELF fluctuations. For $k\rho_i > 1$ and $k\rho_s < 1$, BB-ELF emissions are wavelike and have a , k^{-5} power law. For $k\rho_s > 1$, observed BB-ELF are spatial structures that are not well described by plane waves and have a k^{-2} power law.

The open questions from this event are as follows; what is the causal rela-

tionship between the larger scale Alfén waves and the steepened electric field structures, and what generates the kilometer scale structure? How do the ions and plasma density respond and evolve with respect to the separate scale BB-ELF waves? What is the exact wave-frequency/wave-vector dispersion relationship and how is the observed electric field power spectral density related the plasma frame turbulence?

CHAPTER 4

CONCLUSIONS AND FUTURE WORK

This thesis presented three different applications of a multi-point and multi-payload sounding rocket mission to study auroral plasma physics. Chapter 1 showed how knowledge of vector quantities, in that case the electric field, can be used to estimate spatial gradients. Previous rocket and satellite missions assumed that all variations in the spacecraft frame were due to the spacecraft passing through spatial structure. Chapter 1 compared direct measurements of velocity shear to traditional single point measurements, and showed that traditional measurements can be in error by a factor of two. Chapter 2 used both single payload and multi-payload interferometry to measure the parallel and perpendicular wavelength of VLF hiss, a ubiquitous auroral emission, to show it falls on the whistler wave resonance cone. Finally, Chapter 3 used a wavelet based frequency/wavevector decomposition to show that the motion of medium scale optical auroral features correlates with the motion of medium scale magnetohydrodynamic structures rather than the local plasma drift velocity.

With the launch of the Polar, FAST and CLUSTER satellite missions Alfvénic aurora, the topic of Chapter 3, has received considerable experimental attention. Due primarily to FAST, the physics of Alfvén waves and structures in the auroral acceleration region are fairly well understood. However, electric and magnetic field measurements below $\sim$ 1000km are rare leaving hole in our understanding of the physics of Alfvén waves and structures in this region and below. This region is particularly important as a source for magnetospheric O^+, and the results of Chapter 3 show that this region can be a dominant source of

auroral electrons. Open questions remain, however, about the exact processes responsible for O^+ energization. The primary concern in determining the character and instabilities behind the ubiquitous co-observation of BB-ELF waves and heated O^+. Originally, it was thought that current-driven (parallel electron drift) cyclotron and ion-acoustic waves were primarily responsible for BB-ELF and ion energization [*Kindel and Kennel*, 1971]. Two types of observations show the limitations of current-driven instabilities, 1) auroral zone field aligned currents are generally too low to destabilize current-driven plasma waves, and 2) there are an extremely limited number of wave observations with structure at the O^+ cyclotron frequency. Two competing classes of instability have been proposed to explain BB-ELF. The first are broadly termed the inhomogeneous-energy-density-driven instabilities reviewed in *Amatucci* [1999], and are related to sheared electric fields (plasma velocity) and are broadband temporal emissions. The second are current-shear-driven instabilities, which can explain both auroral structuring *Seyler* [1990] and BB-ELF plasma wave emission and are characterized as low-frequency plasma structures.

Spacecraft based plasma wave measurements are plagued with the space-time ambiguity where spatial waves and structures will be doppler shifted due to spacecraft motion such that the observed frequency, $f_{sc} = f_{wave} - \mathbf{k} \cdot \mathbf{v}_{sc}$. For the Cascades2 sounding rocket mission there were two ambiguous frequency/wavenumber ranges. The first occurred at $f_{sc} \sim 8$Hz and would correspond to a Doppler shifted wavelength of ~ 180m which is near electron inertial length $2\pi\lambda_e$. The second occurred at $f_{sc} \sim 40$Hz which is near the O^+ gyrofrequency and would correspond to a Doppler shifted wavelength of 37m, near the gyroradius at electron temperature, $2\pi\rho_s$.

As shown in paper 2, interferometry can be a powerful tool to resolve the space-time ambiguity, but the observable wave numbers are limited to the range $|kd| \leq \pi$, or $\lambda \geq 2d$, where d is the sensor separation distance. In addition to this effective lower bound on observable wave length, there exists a qualitative upper bound on observable wavelength which is related to sampling rates, spacecraft frame frequencies, payload separation, and noise. To probe the wavelengths in the electron inertial range of ~100m, payload separation would need to be on the order of some 10's of meters. Due to the length of the wirebooms, this is a experimentally difficult configuration to achieve as it would require low payload separation velocities, significantly less than 1m/s, and would require careful maneuvers after subpayload ejection to avoid collisions.

The Cornell rocket program has had considerable success probing ~40m ($f_{sc} \sim$ 40Hz) range using the sphere-to-skin channels VLF wave receivers and "double-double" probes (see *Bonnell* [1997] for a full discussion of double-double probe response) . The 12 sphere pair on each Cascades2 subpayload was equipped with a pre-amplifier connected to an HF wave receiver. These pre-amps interfered with the VLF gain by a factor of two. The sphere-to-skin channels are significantly noisier than sphere-to-sphere channels. An obvious advance for the Cowboy subpayloads would be the addition of a double-double probe system. The polarization observations of Chapter 3 showed that above f_{sc} = 40Hz the orthogonal electric fields failed to maintain a consistent phase relationship, ie, were spatial, possible vortical structures. As shown in Chapter 2, the interpretation of interferometric measurements depends on the wave model, if the observed instability isn't a wave interferometric observations may fail to be coherent. This may explain why *Kintner et al.* [2000] observed low coherency over many 100s of BB-ELF plasma wave emissions.

BIBLIOGRAPHY

Amatucci, W. E., Inhomogeneous plasma flows: A review of in situ observations and laboratory experiments, *Journal of Geophysical Research*, *104*, 14,481–14,504, 1999.

Andre, M., and A. Yau, Theories and Observations of Ion Energization and Outflow in the High Latitude Magnetosphere, *Space Science Reviews*, *80*, 27–48, 1997.

André, M., P. Norqvist, L. Andersson, L. Eliasson, A. I. Eriksson, L. Blomberg, R. E. Erlandson, and J. Waldemark, Ion energization mechanisms at 1700 km in the auroral region, *Journal of Geophysical Research*, *103*, 4199–4222, 1998.

Bering, E. A., M. C. Kelley, and F. S. Mozer, Observations of an intense field-aligned thermal ion flow and associated intense narrow band electric field oscillations, *Journal of Geophysical Research*, *80*, 4612–4620, 1975.

Bonnell, J. W., Identification of broadband ELF waves observed during transverse ion acceleration in the auroral ionosphere, Ph.D. thesis, CORNELL UNIVERSITY, 1997.

Buchsbaum, S. J., Resonance in a Plasma with Two Ion Species, *Physics of Fluids*, *3*, 418–420, 1960.

Cattell, C., and M. Hudson, Flute mode waves near the lower hybrid frequency excited by ion rings in velocity space, *Geophysical Research Letters*, *9*, 1167–1170, 1982.

Chaston, C. C., J. W. Bonnell, C. W. Carlson, M. Berthomier, L. M. Peticolas, I. Roth, J. P. McFadden, R. E. Ergun, and R. J. Strangeway, Electron accelera-

tion in the ionospheric Alfven resonator, *Journal of Geophysical Research (Space Physics)*, *107*, 1413, 2002a.

Chaston, C. C., J. W. Bonnelll, C. W. Carlson, J. P. McFadden, R. E. Ergun, and R. J. Strangeway, Ion Acceleration in Alfven Waves Above the Aurora From FAST, *AGU Fall Meeting Abstracts*, pp. C5+, 2002b.

Chaston, C. C., L. M. Peticolas, J. W. Bonnell, C. W. Carlson, R. E. Ergun, J. P. McFadden, and R. J. Strangeway, Width and brightness of auroral arcs driven by inertial Alfven waves, *Journal of Geophysical Research (Space Physics)*, *108*, 1091, 2003.

Chaston, C. C., C. W. Carlson, J. P. McFadden, R. E. Ergun, and R. J. Strangeway, How important are dispersive Alfvén waves for auroral particle acceleration?, *Geophysical Research Letters*, *34*, L07,101, 2007.

Chaston, C. C., C. Salem, J. W. Bonnell, C. W. Carlson, R. E. Ergun, R. J. Strangeway, and J. P. McFadden, The Turbulent Alfvénic Aurora, *Physical Review Letters*, *100*, 175,003–+, 2008.

Chaston, C. C., K. Seki, T. Sakanoi, K. Asamura, and M. Hirahara, Motion of aurorae, *Geophysical Research Letters*, *37*, 8104–+, 2010.

Chaston, C. C., et al., Energy deposition by Alfvén waves into the dayside auroral oval: Cluster and FAST observations, *Journal of Geophysical Research (Space Physics)*, *110*, A02,211, 2005a.

Chaston, C. C., et al., Drift-Kinetic Alfvén Waves Observed near a Reconnection X Line in the Earth's Magnetopause, *Physical Review Letters*, *95*, 065,002–+, 2005b.

Clark, A. E., and C. E. Seyler, Electron beam formation by small-scale oblique inertial Alfvén waves, *Journal of Geophysical Research*, *104*, 17,233–17,250, 1999.

Dudok de Wit, T., V. V. Krasnosel'skikh, S. D. Bale, M. W. Dunlop, H. Lühr, S. J. Schwartz, and L. J. C. Woolliscroft, Determination of dispersion relations in quasi-stationary plasma turbulence using dual satellite data, *Geophysical Research Letters*, *22*, 2653–2656, 1995a.

Dudok de Wit, T., V. V. Krasnosel'skikh, S. D. Bale, M. W. Dunlop, H. Lühr, S. J. Schwartz, and L. J. C. Woolliscroft, Determination of dispersion relations in quasi-stationary plasma turbulence using dual satellite data, *Geophysical Research Letters*, *22*, 2653–2656, 1995b.

Earle, G. D., and M. C. Kelley, Spectral evidence for stirring scales and two-dimensional turbulence in the auroral ionosphere, *Journal of Geophysical Research*, *98*, 11,543–+, 1993.

Earle, G. D., M. C. Kelley, and G. Ganguli, Large velocity shears and associated electrostatic waves and turbulence in the auroral F region, *Journal of Geophysical Research*, *94*, 15,321–15,333, 1989.

Eliasson, L., et al., Freja observations of heating and precipitation of positive ions, *Geophysical Research Letters*, *21*, 1911–1914, 1994.

Ergun, R. E., E. Klementis, C. W. Carlson, J. P. McFadden, and J. H. Clemmons, Wavelength measurement of auroral hiss, *Journal of Geophysical Research*, *96*, 21,299–+, 1991.

Farley, D. T., H. M. Ierkic, and B. G. Fejer, Radar interferometry - A new technique for studying plasma turbulence in the ionosphere, *Journal of Geophysical Research*, *86*, 1467–1472, 1981.

Fisher, R. K., and R. W. Gould, Resonance Cones in the Field Pattern of a Radio Frequency Probe in a Warm Anisotropic Plasma, *Physics of Fluids*, *14*, 857–867, 1971.

Fredricks, R. W., and F. V. Coroniti, Ambiguities in the deduction of rest frame fluctuation spectrums from spectrums computed in moving frames, *Journal of Geophysical Research*, *81*, 5591–5595, 1976.

Ganguli, G., Y. C. Lee, and P. J. Palmadesso, Kinetic theory for electrostatic waves due to transverse velocity shears, *Physics of Fluids*, *31*, 823–838, 1988.

Ganguli, G., M. J. Keskinen, H. Romero, R. Heelis, T. Moore, and C. Pollock, Coupling of microprocesses and macroprocesses due to velocity shear: An application to the low-altitude ionosphere, *Journal of Geophysical Research*, *99*, 8873–8889, 1994.

Gavrishchaka, V. V., M. E. Koepke, and G. I. Ganguli, Ion cyclotron modes in a two-ion-component plasma with transverse-velocity shear, *Journal of Geophysical Research*, *102*, 11,653–11,664, 1997.

Gavrishchaka, V. V., G. I. Ganguli, W. A. Scales, S. P. Slinker, C. C. Chaston, J. P. McFadden, R. E. Ergun, and C. W. Carlson, Multiscale Coherent Structures and Broadband Waves due to Parallel Inhomogeneous Flows, *Physical Review Letters*, *85*, 4285–4288, 2000.

Goertz, C. K., and R. W. Boswell, Magnetosphere-ionosphere coupling, *Journal of Geophysical Research*, *84*, 7239–7246, 1979.

Gurnett, D. A., and L. A. Frank, VLF Hiss and Related Plasma Observations in the Polar Magnetosphere, *Journal of Geophysical Research*, *77*, 172–190, 1972.

Hallinan, T., The Distribution of Vorticity in Auroral Arcs, in *Physics of Auroral Arc Formation, Geophysical Monograph 25*, edited by S.-I. Akasofu & J. R. Kan, pp. 42–+, 1981.

Hui, C.-H., and C. E. Seyler, Electron acceleration by Alfven waves in the magnetosphere, *Journal of Geophysical Research*, *97*, 3953–3963, 1992.

Humphreys, T. E., L. Psiaki, M., E. M. Klatt, S. P. Powell, and P. M. Kintner, Magnetometer-Based Attitude and Rate Estimation for Spacecraft with Wire Booms, *Journal of Guidance, Control, and Dynamics*, *28*, 584–593, 2005.

Kelley, M. C., and C. W. Carlson, Observations of intense velocity shear and associated electrostatic waves near an auroral arc, *Journal of Geophysical Research*, *82*, 2343–2348, 1977.

Kelley, M. C., and F. S. Mozer, A Satellite Survey of Vector Electric Fields in the Ionosphere at Frequencies of 10 to 500 Hertz, 1. Isotropic, High-Latitude Electrostatic Emissions, *Journal of Geophysical Research*, *77*, 4158–4173, 1972.

Kindel, J. M., and C. F. Kennel, Topside Current Instabilities, *Journal of Geophysical Research*, *76*, 3055–3078, 1971.

Kintner, P. M., M. C. Kelley, G. Holmgren, H. Koskinen, and G. Gustafsson, Detection of spatial density irregularities with the Viking plasma wave interferometer, *Geophysical Research Letters*, *14*, 467–470, 1987.

Kintner, P. M., W. Scales, J. Vago, R. Arnoldy, G. Garbe, and T. Moore, Simultaneous observations of electrostatic oxygen cyclotron waves and ion conics, *Geophysical Research Letters*, *16*, 739–742, 1989.

Kintner, P. M., J. Vago, W. Scales, A. Yau, B. Whalen, R. Arnoldy, and T. Moore, Harmonic H(+) gyrofrequency structures in auroral hiss observed by high-

altitude auroral sounding rockets, *Journal of Geophysical Research*, *96*, 9627–9638, 1991.

Kintner, P. M., J. Vago, S. Chesney, R. L. Arnoldy, K. A. Lynch, C. J. Pollock, and T. E. Moore, Localized lower hybrid acceleration of ionospheric plasma, *Physical Review Letters*, *68*, 2448–2451, 1992.

Kintner, P. M., J. Bonnell, R. Arnoldy, K. Lynch, C. Pollock, and T. Moore, SCIFER-Transverse ion acceleration and plasma waves, *Geophysical Research Letters*, *23*, 1873–1876, 1996.

Kintner, P. M., J. Franz, P. Schuck, and E. Klatt, Interferometric coherency determination of wavelength or what are broadband ELF waves?, *Journal of Geophysical Research*, *105*, 21,237–21,250, 2000.

Kintner, P. M., Jr., Observations of velocity shear driven plasma turbulence, *Journal of Geophysical Research*, *81*, 5114–5122, 1976.

Klatt, E. M., P. M. Kintner, C. E. Seyler, K. Liu, E. A. MacDonald, and K. A. Lynch, SIERRA observations of Alfvénic processes in the topside auroral ionosphere, *Journal of Geophysical Research (Space Physics)*, *110*, A10S12, 2005.

Kletzing, C. A., Electron acceleration by kinetic Alfvén waves, *Journal of Geophysical Research*, *99*, 11,095–11,104, 1994.

Kletzing, C. A., and S. Hu, Alfvén wave generated electron time dispersion, *Geophysical Research Letters*, *28*, 693–696, 2001.

Knudsen, D. J., M. C. Kelley, and J. F. Vickrey, Alfven waves in the auroral ionosphere - A numerical model compared with measurements, *Journal of Geophysical Research*, *97*, 77–90, 1992.

Knudsen, D. J., J. H. Clemmons, and J. Wahlund, Correlation between core ion energization, suprathermal electron bursts, and broadband ELF plasma waves, *Journal of Geophysical Research*, *103*, 4171–4186, 1998a.

Knudsen, D. J., J. H. Clemmons, and J.-E. Wahlund, Correlation between core ion energization, suprathermal electron bursts, and broadband ELF plasma waves, *Journal of Geophysical Research*, *103*, 4171–4186, 1998b.

Labelle, J., and P. M. Kintner, The measurement of wavelength in space plasmas, *Reviews of Geophysics*, *27*, 495–518, 1989.

LaBelle, J., and R. A. Treumann, Auroral Radio Emissions, 1. Hisses, Roars, and Bursts, *Space Science Reviews*, *101*, 295–440, 2002.

Liu, K., C. E. Seyler, and T. Xu, Particle-in-cell simulations of current shear-driven instabilities and the generation of broadband ELF fluctuations, *Journal of Geophysical Research (Space Physics)*, *111*, 11,307–+, 2006.

Lund, E. J., and J. LaBelle, On the generation and propagation of auroral electromagnetic ion cyclotron waves, *Journal of Geophysical Research*, *102*, 17,241–17,254, 1997.

Lundberg, T., E., M. Kintner, P., A. Lynch, K., and R. Mella, M.

Lynch, K. A., J. W. Bonnell, C. W. Carlson, and W. J. Peria, Return current region aurora: $E_{\|}$, j_z, particle energization, and broadband ELF wave activity, *Journal of Geophysical Research (Space Physics)*, *107*, 1115–+, 2002.

Lynch, K. A., M. R. Mella, D. Hampton, H. C. Stenbaek-Nielsen, H. Dahlgren, M. Disbrow, P. M. Kintner, and E. T. Lessard, M. andLundberg, Structure and dynamics of auroral electron precipitation: sounding rocket and groundbased

observations of tall rays at the nightside poleward boundary, *Journal of Geophysical Research*, 2011, to be submitted to *Journal of Geophysical Research*.

Lysak, R. L., Auroral electrodynamics with current and voltage generators, *Journal of Geophysical Research*, *90*, 4178–4190, 1985.

Lysak, R. L., Feedback instability of the ionospheric resonant cavity, *Journal of Geophysical Research*, *96*, 1553–1568, 1991.

Maggs, J. E., Coherent generation of VLF hiss, *Journal of Geophysical Research*, *81*, 1707–1724, 1976.

Mallinckrodt, A. J., and C. W. Carlson, Relations between transverse electric fields and field-aligned currents, *Journal of Geophysical Research*, *83*, 1426–1432, 1978.

Mella, M. R., K. A. Lynch, P. M. Kintner, E. T. Lundberg, M. Lessard, D. L. Hampton, and H. Stenbaek-Nielsen, H. C. Dahlgren, Sounding Rocket Study of an auroral poleward boundary intensification.

Mosier, S. R., and D. A. Gurnett, Ionospheric Observation of VLF Electrostatic Noise related to Harmonics of the Proton Gyrofrequency, *Nature*, *223*, 605–606, 1969.

Pincon, J. L., and F. Lefeuvre, The application of the generalized Capon method to the analysis of a turbulent field in space plasma - Experimental constraints, *Journal of Atmospheric and Terrestrial Physics*, *54*, 1237–1247, 1992.

Powell, S. P., M. Klatt, E., and P. M. Kintner, Plasma Wave Interferometry using GPS position and timing on a formation of three sub-orbital payloads, in *ION GPS 2002*, Institute of Navigation, Portland, Oregon, 2002.

Psiaki, L., M., Attitude-Determination Filtering via Extended Quaternion Estimation, *Journal of Guidance, Control, and Dynamics*, *23*, 206–214, 2002.

Romero, H., and G. Ganguli, Nonlinear evolution of a strongly sheared cross-field plasma flow, *Physics of Fluids B*, *5*, 3163–3181, 1993.

Samson, J. C., and J. V. Olson, Some comments on the descriptions of the polarization states of waves, *Geophysical Journal International*, *61*, 115–129, 1980.

Schuck, P. W., C. E. Seyler, J.-L. Pinçon, J. W. Bonnell, and P. M. Kintner, Theory, simulation, and observation of discrete eigenmodes associated with lower hybrid solitary structures, *Journal of Geophysical Research*, *103*, 6935–6954, 1998.

Schuck, P. W., J. W. Bonnell, and P. M. Kintner, A review of lower hybrid solitary structures, *IEEE Transactions on Plasma Science*, *31*, 1125–1177, 2003.

Semeter, J., and E. M. Blixt, Evidence for Alfvén wave dispersion identified in high-resolution auroral imagery, *Geophysical Research Letters*, *33*, L13,106, 2006.

Seyler, C. E., A mathematical model of the structure and evolution of small-scale discrete auroral arcs, *Journal of Geophysical Research*, *95*, 17,199–17,215, 1990.

Seyler, C. E., and K. Liu, Particle energization by oblique inertial Alfvén waves in the auroral region, *Journal of Geophysical Research (Space Physics)*, *112*, A09,302, 2007.

Seyler, C. E., and J.-E. Wahlund, Theory of nearly perpendicular plasma waves and comparison to Freja satellite observations, *Journal of Geophysical Research*, *101*, 21,795–21,813, 1996.

Seyler, C. E., and K. Wu, Instability at the electron inertial scale, *Journal of Geophysical Research*, *106*, 21,623–21,644, 2001.

Seyler, C. E., J.-E. Wahlund, and B. Holback, Theory and simulation of low-frequency plasma waves and comparison to Freja satellite observations, *Journal of Geophysical Research*, *100*, 21,453–21,472, 1995.

Seyler, C. E., A. E. Clark, J. Bonnell, and J.-E. Wahlund, Electrostatic broadband ELF wave emission by Alfvén wave breaking, *Journal of Geophysical Research*, *103*, 7027–7042, 1998.

Seyler, C. E., Jr., Nonlinear 3-D evolution of bounded kinetic Alfven waves due to shear flow and collisionless tearing instability, *Geophysical Research Letters*, *15*, 756–759, 1988.

Smith, R. L., and N. Brice, Propagation in Multicomponent Plasmas, *Journal of Geophysical Research*, *69*, 5029–5040, 1964.

Spreiter, J. R., and B. R. Briggs, Theory of Electrostatic Fields in the Ionosphere at Polar and Middle Geomagnetic Latitudes, *Journal of Geophysical Research*, *66*, 1731–1744, 1961.

Stasiewicz, K., Y. Khotyaintsev, M. Berthomier, and J.-E. Wahlund, Identification of widespread turbulence of dispersive Alfvén waves, *Geophysical Research Letters*, *27*, 173–176, 2000a.

Stasiewicz, K., et al., Small Scale Alfvénic Structure in the Aurora, *Space Science Reviews*, *92*, 423–533, 2000b.

Streltsov, A., and W. Lotko, Dispersive field line resonances on auroral field lines, *Journal of Geophysical Research*, *100*, 19,457–19,472, 1995.

Sundkvist, D., V. Krasnoselskikh, P. K. Shukla, A. Vaivads, M. André, S. Buchert, and H. Rème, In situ multi-satellite detection of coherent vortices as a manifestation of Alfvénic turbulence, *Nature*, *436*, 825–828, 2005.

Trondsen, T. S., and L. L. Cogger, A survey of small-scale spatially periodic distortions of auroral forms, *Journal of Geophysical Research*, *103*, 9405–9416, 1998.

Voitenko, Y., and J. De Keyser, Turbulent spectra and spectral kinks in the transition range from MHD to kinetic Alfv\'en turbulence, *ArXiv e-prints*, 2011.

Voitenko, Y. M., Three-wave coupling and weak turbulence of kinetic Alfvén waves, *Journal of Plasma Physics*, *60*, 515–527, 1998.

Wahlund, J.-E., et al., Broadband ELF plasma emission during auroral energization 1. Slow ion acoustic waves, *Journal of Geophysical Research*, *103*, 4343–4376, 1998.

Watt, C. E. J., R. Rankin, I. J. Rae, and D. M. Wright, Self-consistent electron acceleration due to inertial Alfvén wave pulses, *Journal of Geophysical Research (Space Physics)*, *110*, A10S07, 2005.